Subscale Tiltrotor eVTOL Aircraft Dynamic Modeling and Flight Control Software Development

Benjamin M. Simmons

Research Aerospace Engineer Flight Dynamics Branch

Garrett D. Asper

Pathways Intern Flight Dynamics Branch

Steven M. Snyder

Research Aerospace Engineer Dynamic Systems and Control Branch

Steven C. Geuther

Aerospace Engineer Aeronautics Systems Engineering Branch

Kasey A. Ackerman

Research Aerospace Engineer Dynamic Systems and Control Branch

Matthew N. Gray

Electronics Engineer
Aeronautics Systems Engineering Branch

Rachel M. Axten

Pathways Intern Dynamic Systems and Control Branch

Ryan Chan

Electronics Engineer Aeronautics Systems Engineering Branch

NASA Langley Research Center Hampton, VA, USA

ABSTRACT

This paper describes the dynamic modeling and flight control software development efforts for a subscale tiltrotor electric vertical takeoff and landing (eVTOL) aircraft built at NASA Langley Research Center. The vehicle, referred to as the Research Aircraft for eVTOL Enabling techNologies (RAVEN) Subscale Wind-Tunnel and Flight Test (SWFT) model, serves as a flight dynamics and controls research testbed to foster advances in eVTOL aircraft technology. After fabricating the vehicle, wind-tunnel testing was conducted to identify a high-fidelity aero-propulsive model for use in a flight dynamics simulation enabling flight control system development. The RAVEN-SWFT aircraft subsequently underwent flight-test risk reduction steps and then free flight testing employing custom research flight control software. The flight control software, which can be efficiently updated and tested on the vehicle, includes a robust model-based control algorithm and an extensive programmed test input injection capability. The progress of RAVEN-SWFT research activities will be summarized alongside the associated modeling and flight control software development aspects, including the flight dynamics simulation, flight control system architecture, vehicle integration, and testing approaches.

INTRODUCTION

Many complex distributed hybrid and electric propulsion aircraft concepts are being investigated to enable future Advanced Air Mobility (AAM) transportation missions (Refs. 1–6). There are numerous vertical takeoff and landing (VTOL), short takeoff and landing (STOL), and conventional takeoff and landing (CTOL) configurations with vast Urban Air Mobility (UAM) and Regional Air Mobility (RAM) applications. Ubiquitous characteristics of these novel aircraft include the use of many distributed propulsors and control surfaces, as well as significant aero-propulsive coupling.

Presented at the Vertical Flight Society's 81st Annual Forum & Technology Display, Virginia Beach, VA, USA, May 20–22, 2025. This material is declared a work of the U.S. Government and is not subject to copyright protection in the United States.

Vehicles designed for UAM missions require precise hover and efficient cruise capabilities, as well as the ability to safely transition between flight regimes; electric VTOL aircraft are a promising candidate to fulfill future UAM operations. In general, eVTOL aircraft are a combination of traditional fixedwing and rotary-wing aircraft leveraging certain attributes from each type of vehicle. Fixed-wing aircraft provide longer endurance, better efficiency, and the ability to operate at high speeds, whereas rotary-wing aircraft offer the ability to take-off and land vertically, hover, and precisely maneuver in confined areas. New distributed propulsion technology that is used in many eVTOL vehicles has further expanded the traditional aircraft design space and has yielded a multitude of unique vehicle designs. As of March 2025, there are 1,100 known eVTOL aircraft concepts (Ref. 7).

Although widespread use of eVTOL aircraft has great po-

tential, many open research areas need to be addressed prior to introduction into a UAM transportation environment. One essential research area is accurate eVTOL vehicle aeropropulsive modeling enabling flight dynamics simulation development. Another critical eVTOL aircraft research area, which substantially benefits from an accurate flight dynamics simulation, is flight control system development. Together, the delivery of a high-fidelity flight dynamics model and effective flight control system enable both accurate flight simulations and successful flight testing, which facilitates research in many other areas including airworthiness certification, air traffic management, pilot-operator interface, handling qualities, simplified vehicle operations, contingency management, and autonomous systems. Efficient, accurate aero-propulsive model development and robust, well-performing flight control system design, however, is challenged by several eV-TOL vehicle attributes, including: many control surfaces and propulsors, propulsion-airframe interactions, vehicle instability, and rapidly changing aerodynamics through large operational flight envelopes. Previous related research has investigated methods for rapid, high-fidelity eVTOL aircraft aeropropulsive modeling across their wide flight envelopes using computational predictions (Refs. 8, 9), wind-tunnel testing (Refs. 10–16), and flight-test approaches (Refs. 17, 18). In parallel, full-envelope flight control system development approaches for complex transitioning eVTOL aircraft have been explored (e.g., Refs. 19-24).

The present work describes the modeling and flight control software development methods applied for a subscale tiltrotor eVTOL aircraft to realize the project's research objectives. Furthermore, the control algorithm design approach and testing efforts are summarized. The paper strives to present the software development and testing techniques with sufficient detail to allow for the methods to be used to help collectively advance the state-of-the-art of eVTOL aircraft technology.

The paper is organized as follows. First, an overview is provided of the experimental eVTOL aircraft. Next, the wind-tunnel testing and aero-propulsive modeling efforts are summarized, followed by a description of the flight dynamics simulation. Subsequent sections detail the flight control system design, programmed test input injection capabilities, and flight control system integration methods. The paper closes with a discussion of software assurance and airworthiness considerations, the flight-test approach being applied for the vehicle, and concluding remarks.

AIRCRAFT

To help study the aforementioned eVTOL aircraft research areas, NASA Langley Research Center (LaRC) has built the Research Aircraft for eVTOL Enabling techNologies (RAVEN) Subscale Wind-Tunnel and Flight Test (SWFT) model (Ref. 25). The RAVEN-SWFT is a 28.6% scale version of the RAVEN 1000-lb class eVTOL aircraft concept (Ref. 26), which was designed in a collaborative effort between NASA LaRC and the Georgia Institute of Technology (Georgia Tech). The RAVEN aircraft is a tiltrotor eV-

TOL configuration with six variable-pitch proprotors. The front four proprotors tilt forward and are operational throughout the entire flight envelope. The rear two proprotors do not tilt and serve as lifting proprotors in hover and transition. The aircraft control surfaces include six flaperons, a stabilator, and a rudder. In total, the vehicle has 24 independent control effectors:

- Six proprotor rotational speeds $(n_1, n_2, ..., n_6)$
- Six proprotor collective pitch angles $(\delta_{c_1}, \delta_{c_2}, ..., \delta_{c_6})$
- Four nacelle tilt angles $(\delta_{t_1}, \delta_{t_2}, \delta_{t_3}, \delta_{t_4})$
- Six flaperon deflection angles $(\delta_{f_1}, \delta_{f_2}, ..., \delta_{f_6})$
- One stabilator deflection angle (δ_s)
- One rudder deflection angle (δ_r)

Figure 1 shows a schematic of the RAVEN aircraft with annotations showing the vehicle propulsor and control surface definitions.

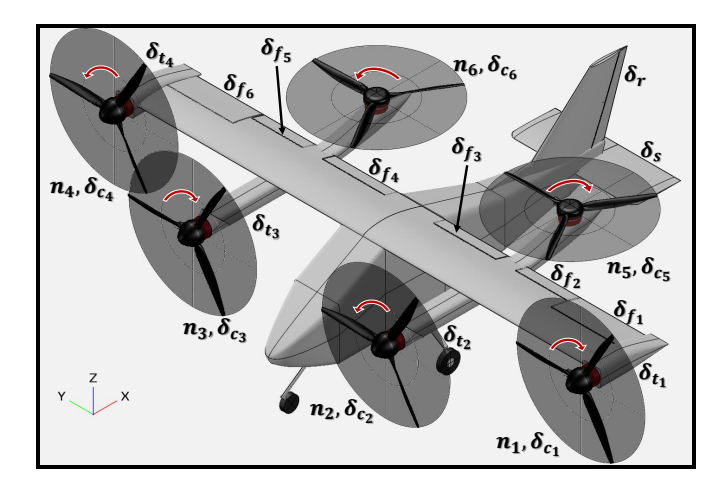


Figure 1: RAVEN control effector definitions.

The RAVEN-SWFT, pictured in the NASA LaRC 12-Foot Low-Speed Tunnel (LST) (Ref. 27) in Fig. 2, was designed as a flight dynamics and controls research testbed to advance eVTOL aircraft technology and help bring similar full-scale vehicles into mainstream operation. As its name suggests, the vehicle is designed for use in both wind-tunnel and flight-test experiments. The aircraft has a flight weight of 38 pounds, a wingspan of 5.7 ft (excluding the outboard tilt nacelles), and a proprotor diameter of 19.5 inches. The current RAVEN-SWFT moments of inertia and product of inertia estimates, experimentally determined using both torsional and compound pendulum methods, are provided in Ref. 25.

The RAVEN-SWFT was developed as NASA LaRC's latest and most capable subscale eVTOL research aircraft. Two predecessor subscale eVTOL aircraft were the GL-10 (Ref. 28) and LA-8 (Refs. 29, 30). The GL-10 was a subscale, tiltwing, tilt-tail VTOL aircraft. Several scaled variants of the GL-10 vehicle were developed and tested, which enabled research in wind-tunnel testing (Refs. 10, 11), flight controls (Ref. 31), and flight testing (Refs. 32,33). The LA-8 was a subscale, tandem tiltwing VTOL aircraft built as a wind-tunnel and flight testbed for eVTOL aircraft technology. The LA-8 project enabled research in rapid vehicle development (Refs. 29,



(a) Front view (cruise configuration)



(b) Overhead view (hover configuration)



(c) Side view (mid-transition configuration)

Figure 2: RAVEN-SWFT mounted in the NASA LaRC 12-Foot Low-Speed Tunnel. (Credit: NASA)

30), computational aerodynamic predictions (Refs. 34–36), wind-tunnel testing (Refs. 12, 37), high incidence angle propeller aerodynamics (Refs. 38–40), aero-propulsive modeling (Refs. 13, 14, 41), flight controls (Ref. 19), and flight-test strategies (Ref. 17). The GL-10 and LA-8 both had successful wind-tunnel and flight-test campaigns that yielded numerous eVTOL aircraft research advances; however, due to budgetary constraints and programmatic adjustments, neither project fulfilled the research goal of testing custom flight control software throughout the full flight envelope, leaving an important open flight-test research area unexplored. From its initial conceptualization, the RAVEN-SWFT aircraft was designated to continue eVTOL aircraft research pursuits started on the GL-10 and LA-8, with a key focus on creating a testbed for ad-

vanced modeling and flight controls research. Accordingly, a large emphasis was placed on being able to rapidly design, integrate, test, and refine custom flight control algorithms.

A significant emphasis of the RAVEN project has been on public dissemination of methods and data to foster advancement of the eVTOL aircraft industry. Reference 25 provides a summary of past, current, and future research efforts being pursued by the RAVEN-SWFT project, which includes isolated proprotor characterization (Ref. 42), static poweredairframe wind-tunnel testing and aero-propulsive model development (Ref. 15), computational aerodynamics predictions (Ref. 43), and aerodynamic damping estimation from free motion wind-tunnel testing (Ref. 16). The RAVEN-SWFT wind-tunnel testing efforts are summarized in the next section to provide context and explain their purpose for the present application. The current paper focuses on the modeling and flight control software development enabling flight-test research conducted using the RAVEN-SWFT vehicle. This substantial software development effort has only been mentioned glancingly in previous publications and, thus, forms the primary emphasis and new contributions of this paper.

WIND-TUNNEL TESTING AND AERO-PROPULSIVE MODELING

Wind-tunnel tests performed in the NASA LaRC 12-Foot LST for RAVEN-SWFT enabled identification of an accurate aeropropulsive model used for flight dynamics simulation development and model-based flight control system design. The static wind-tunnel test campaign included characterizing the isolated proprotor (Ref. 42), the isolated airframe (without proprotors), and powered airframe (with proprotors operating) (Ref. 15). Design of experiments (DOE) and response surface methodology (RSM) test techniques (Refs. 44, 45) were applied throughout static wind-tunnel testing (Ref. 15). In contrast to traditional one-factor-at-a-time testing, experiments planned using DOE/RSM theory efficiently scale for a large number of test factors, which is essential for characterizing the complex nonlinear aerodynamics and interactions present with eVTOL aircraft. DOE/RSM techniques increase the productivity of data collection by simultaneously varying all test factors in a way that allows efficient determination of the individual contribution of each individual factor, as well as interaction effects among test factors, while fundamentally providing a statistically-rigorous experiment design approach. RAVEN-SWFT is the first eVTOL vehicle tested at NASA LaRC to primarily apply DOE/RSM techniques throughout its static wind-tunnel testing.

The RAVEN-SWFT static wind-tunnel testing yielded the data needed to identify a high-fidelity static transition model; however, aerodynamic damping effects are not characterized in static testing and are required to accurately predict aircraft motion in dynamic maneuvering with nonzero angular velocity. Forced oscillation testing (Refs. 46, 47) is a traditional dynamic wind-tunnel test technique used to characterize aerodynamic damping by forcing the dynamic motion

of a wind-tunnel model; however, due to the significant aircraft complexity and large number of operating conditions, applying this approach to eVTOL vehicles would be very time consuming. Instead, to increase the efficiency of dynamic wind-tunnel testing, three degree-of-freedom (3DOF) free motion wind-tunnel testing was used to characterize the RAVEN-SWFT aero-propulsive damping effects. Figure 3 shows the RAVEN-SWFT vehicle mounted on a 3DOF apparatus that was recently designed and built at NASA LaRC. In essence, the RAVEN-SWFT 3DOF wind-tunnel testing for aero-propulsive damping characterization was executed by having the flight control system track commanded attitude angles and transition the aircraft based on tunnel dynamic pressure, while also injecting multisine programmed test input excitations to enable collection of informative data for model identification (Ref. 16). As will be discussed later in the paper, the 3DOF testing also allowed for flight control algorithms to be rapidly tested and refined in a low-risk, flight-like environment.



Figure 3: RAVEN-SWFT mounted on a 3DOF free motion wind-tunnel apparatus in the NASA LaRC 12-Foot LST. (Credit: NASA)

After completing wind-tunnel testing, RAVEN-SWFT aeropropulsive models were created from data acquired at several dynamic pressure settings in the transition flight envelope up to 5 lbf/ft² (the practical dynamic pressure limit for testing eVTOL vehicles in the 12-Foot LST). The form of the model is a set of polynomial response surface equations (RSEs). The modeled responses were the dimensional bodyaxis aero-propulsive forces and moments predicted as a function of the body-axis translational velocity, body-axis angular velocity, proprotor rotational speeds, and control effector deflection angles (Refs. 15, 16). To aid in control design, the RSEs were symmetrized by constraining the identification procedures to force control effectors mirrored over the x-z plane to have equal effectiveness and restrict side force, rolling moment, and yawing moment to be zero at zero lateral velocity (sideslip) conditions.

Notably, the high-speed transition and forward flight airspeeds for the RAVEN-SWFT vehicle are higher than the airspeed settings that are able to be tested in the 12-Foot LST. Also, accurate extrapolation of an integrated aero-propulsive vehicle model outside of the test region is difficult due to the significant propulsion, airframe, and interactional contributions to the vehicle aerodynamics. To provide a preliminary estimate of the vehicle aero-propulsive forces and moments at high speeds (i.e., at dynamic pressure values above 5 lbf/ft²), a low-fidelity model was created by superimposing proprotor and isolated airframe models identified from windtunnel testing, which have better independent extrapolation abilities due to their isolated nondimensionalization. This approach ignores interactional aerodynamics, which have a substantial effect; therefore, future computational and/or flighttest model identification is required to produce an accurate aero-propulsive model valid in the high-speed portion of the RAVEN-SWFT flight envelope.

FLIGHT DYNAMICS SIMULATION

A flight dynamics simulation was developed for model-based flight control system design and testing using the RAVEN-SWFT aero-propulsive models. The flight dynamics simulation was developed in Simulink[®] and is a modified version of NASA's open source "Flight Dynamics Simulation of a Generic Transport Model" (Ref. 48), where pertinent changes were made to simulate flight for the RAVEN-SWFT aircraft. The top level of the RAVEN-SWFT simulation Simulink[®] diagram is shown in Fig. 4, which is composed of the simulation inputs, flight control system, vehicle model, and simulation outputs. The inputs, outputs, and vehicle model are described in the following subsections. The flight control system (FCS) is described in the next section.

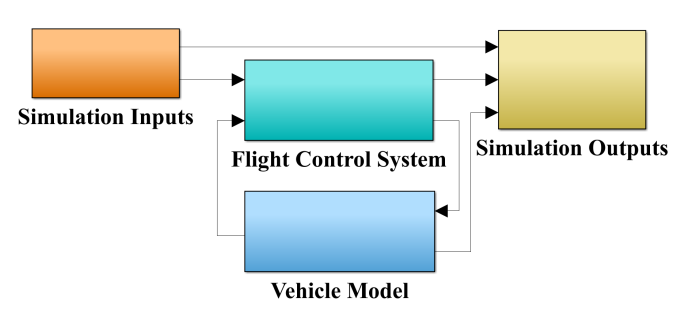


Figure 4: Top-level view of the RAVEN-SWFT simulation Simulink® diagram.

Simulation Inputs

The Simulation Inputs subsystem includes simulated radio control (RC) transmitter inputs, simulated ground control station (GCS) commands, toggleable automatic arming logic for batch simulations, and a simulation elapsed time counter. The

The use of trademarks or names of manufacturers in this report is for accurate reporting and does not constitute an official endorsement, either expressed or implied, of such products or manufacturers by the National Aeronautics and Space Administration.

subsystem is configured to allow for real-time piloted simulations using a USB transmitter for pilot training and assessment of vehicle handling qualities, as well as accelerated automated simulations with input injections for FCS evaluation across the flight envelope. The subsystem is designed to closely emulate the input functionality and structure for the FCS deployed onto the vehicle.

Simulation Outputs

The Simulation Outputs subsystem stores, plots, and creates a visualization of the simulation data. The data from the other subsystems are routed to simulation scopes and stored in the MATLAB® workspace for use by post-processing scripts to facilitate desktop evaluation of the FCS performance and simulation testing to meet software assurance requirements.

The vehicle motion predicted by the flight dynamics simulation can be visualized in real time using a simple generic UAV Animation from the MathWorks® UAV toolbox (Ref. 49) or using a high-fidelity RAVEN-SWFT visualization implemented in X-Plane (Ref. 50), along with a toggleable real-time simulation pacer. The custom RAVEN-SWFT X-Plane visualization includes accurate vehicle geometry and animated control effectors, which is helpful for pilot training, mission rehearsals, and qualitative FCS evaluation. The X-Plane visualization was developed and implemented following the steps given in Ref. 51.

Vehicle Model

The Vehicle Model subsystem includes a control effector dynamics subsystem, a motor performance subsystem, an aero-propulsive model subsystem, an equations of motion subsystem, a sensors subsystem, a ground contact subsystem, and an atmospheric wind/turbulence subsystem. The contents of the vehicle simulation subsystems are highlighted in the following paragraphs.

Control Effector Dynamics The control effector dynamic models describe the control surface servo-actuator position and propulsor rotational speed response subject to changes in the commanded value. Control surface actuation is modeled using a first-order dynamic model, whereas the propulsor rotational speed dynamics are described using a second-order dynamic model. The first- and second-order dynamic models also include a rate limit, time delay, and position limit saturation. Including the rate limit and saturation introduces nonlinearity into the control surface and propulsor dynamic models. Although linear dynamic models are more convenient for control system design and evaluation, including the rate limit and saturation in the model provides a more accurate representation of the actual actuator dynamics in the high-fidelity nonlinear flight dynamics simulation. The control surface and propulsor dynamic model parameters were determined using data collected from step inputs applied to each individual control effector under aerodynamic loading in wind-tunnel testing.

Motor Performance The vehicle motor performance is modeled using RSEs that convert motor rotational speed, collective pitch angle, nacelle tilt angle, and body-axis velocity to motor power consumption. The RSEs were identified using data collected from the isolated proprotor and powered airframe wind-tunnel testing described previously. Although the motor performance models do not influence the vehicle dynamics in the simulation, they help to inform trim strategies and flight-test planning.

Aero-Propulsive Model The aero-propulsive model is composed of the RSEs identified from wind-tunnel testing, as described in the previous section (Refs. 15, 16). The RSEs pertaining to specific dynamic pressure settings are blended using shape-preserving piecewise cubic interpolation (Refs. 52, 53) to form a continuous transition model. After computing the aero-propulsive model predictions as a function of state and control variables, the moment predictions are transferred from the wind-tunnel moment reference center location to the vehicle center of gravity location.

Equations of Motion The equations of motion subsystem includes the kinematic and dynamic aircraft equations of motion developed under a standard set of assumptions (Refs. 54– 56). The aircraft is nominally modeled as a single six-degreeof-freedom (6DOF) rigid body subjected to gravitational force and aero-propulsive forces and moments. The dynamics associated with the rotating portion of each propulsor and nacelle tilt are currently neglected since the inertia of rotating vehicle components is small compared to the overall vehicle inertia; however, multi-body equations of motion (e.g., see Ref. 57) are planned to be added to the nonlinear simulation in the future. The simulation states are the body-axis translational velocity (u, v, w), body-axis angular velocity (p, q, r), attitude quaternions (q_0, q_x, q_y, q_z) , and earth-fixed position in terms of latitude, longitude, and altitude (Φ, Ψ, h) . Because the simulation was used to design a flight controller for a 3DOF windtunnel test, in addition to free flight testing, the 6DOF simulation was programmed to include necessary modifications to conduct 3DOF simulations (Ref. 16).

Sensor Model The simulated sensor data were optionally corrupted with white, Gaussian measurement noise. The sensor model also includes a bias, scale factor, and time delay. The noise properties were determined based on experimental data collected for the RAVEN-SWFT vehicle. The structure of the sensor subsystem closely follows the implementation in Ref. 48.

Ground Contact Model A ground contact model is included to allow simulation of takeoff and landing operations for software verification and pilot training. The current simplified ground contact model is not intended to accurately represent the contact forces and moments of the vehicle landing gear with the ground, but rather is designed to emulate the visual behavior of takeoff/landing operations from a remote pilot

perspective. An accurate physics-based ground contact model is planned to be added in the future.

Atmospheric Model The atmospheric model is identical to subsystems included in Ref. 48, which include the first layer of the 1976 U.S. Standard Atmosphere model (Ref. 58), steady winds, and the Dryden turbulence model (Refs. 59,60). Because the RAVEN-SWFT always operates close to sea level conditions, as currently configured, the aero-propulsive model assumes constant air properties at sea level conditions.

FLIGHT CONTROL SYSTEM DESIGN

The flight control algorithm was developed with a modelbased design approach, using the RAVEN-SWFT flight dynamics simulation. The model-based approach allows for specification of performance and robustness requirements, use of optimal control techniques for gain tuning, rapid development in a simulation environment, and increased confidence in the flight control solutions for vehicle testing (Ref. 61).

The overall RAVEN-SWFT flight control algorithm is composed of a nested-loop architecture, depicted in Fig. 5, including an attitude-control inner loop and a velocity-control outer loop. The design approach includes a linear quadratic integral (LQI) (Ref. 62) model-following control framework with a static feedforward element. The nested-loop architecture allows for sequential design of the flight control laws and multiple entry points for pilot commands, facilitating a build-up approach to flight-test verification. The inner- and outer-loop control laws have the same overall structure, shown in Fig. 6. Each has filtered sensor data used for feedback stabilization and reference tracking, a command model for specifying the desired system response to reference inputs, a static feedforward path for transient response shaping, and a control allocation scheme to appropriately distribute the control system commands.

The following subsections describe the current RAVEN-SWFT trim approach, control allocation, control law design, control modes, and takeoff/landing sequence, as of April 2025. The architecture, parameters, and implementation of the RAVEN-SWFT FCS have continuously evolved as new data have been obtained from wind-tunnel and flight tests. Therefore, it is expected that the FCS will continue to be updated with the collection of new flight-test data and aspects of the control design approach described herein may change in the future.

Trim Approach

The design of the flight control algorithm is based on linearization of the nonlinear flight dynamics simulation at trim conditions. Trim settings, where the sum of gravitational and aero-propulsive forces and moments are equal to zero, were determined across the flight envelope using the constrained nonlinear optimization function fmincon available in MATLAB® (Ref. 49). Trim analysis was performed for

steady, level, unaccelerated flight at different airspeed conditions throughout the transition envelope. To improve the operational practicality and convergence of the trim optimization algorithm, certain control effectors were strategically linked while formulating the optimization problem. The free and/or fixed nonzero variables in the optimization algorithm were:

- Pitch angle, θ (angle of attack, α)
- Front proprotor rotational speed, $n_{\text{front}} = n_1 = n_2 = n_3 = n_4$
- Rear proprotor rotational, $n_{\text{rear}} = n_5 = n_6$
- Front collective pitch angle, $\delta_{c_{\text{front}}} = \delta_{c_1} = \delta_{c_2} = \delta_{c_3} = \delta_{c_4}$
- Rear collective pitch angle, δ_{c_{rear}} = δ_{c5} = δ_{c6}
 Nacelle tilt angle, δ_t = δ_{t1} = δ_{t2} = δ_{t3} = δ_{t4} (except in hover, where nacelle tilt angle was split into outboard nacelle tilt angle $\delta_{t_{\text{out}}} = \delta_{t_1} = \delta_{t_4}$ and inboard nacelle tilt angle $\delta_{t_{\text{in}}} = \delta_{t_2} = \delta_{t_3}$)
- Outboard flap deflection angle, $\delta_{f_{\text{out}}} = \delta_{f_1} = \delta_{f_6}$
- Inboard flap deflection angle, $\delta_{f_{\rm in}} = \delta_{f_2} = \delta_{f_3} = \delta_{f_4} = \delta_{f_5}$
- Stabilator deflection angle, δ_s

Figure 7 shows the free and fixed variable definitions at each flight condition.

The trim optimization objective function was the total motor power usage added to the sum of each motor rotational speed and collective pitch angle in coded units, formed from the operational bounds, raised to an even power. The objective function balances minimizing power consumption (i.e., maximizing vehicle range) and maximizing the available propulsion control authority. Figure 8 provides a visualization of the trim settings for the pitch attitude (θ) , motor rotational speed (n), collective pitch angle (δ_c), nacelle tilt angle (δ_t), flap deflection (δ_f) , and stabilator deflection (δ_s) . The black dotted vertical line at 65 ft/s on each plot represents the limits of the high-fidelity wind-tunnel database. As mentioned previously, the high-speed transition and forward flight airspeeds for the RAVEN-SWFT vehicle are higher than were able to be tested in the 12-Foot LST; accordingly, the high-speed transition model at airspeeds greater than 65 ft/s is lower-fidelity, which increases uncertainty in the trim solution. The trim solutions are expected to be updated after conducting flight testing at these high-speed conditions.

Control Allocation

A weighted pseudo-inverse control allocation approach was used to determine the control effector commands $u_{\rm cmd}$ to achieve desired force and moment commands μ :

$$\boldsymbol{u}_{\text{cmd}} = \boldsymbol{W}^{-1} \bar{\boldsymbol{B}}^{\mathsf{T}} \left(\bar{\boldsymbol{B}} \boldsymbol{W}^{-1} \bar{\boldsymbol{B}}^{\mathsf{T}} \right)^{-1} \boldsymbol{\mu}$$
 (1)

Here, W is a diagonal weighting matrix and \bar{B} is the control effectiveness matrix. Following the approach of Ref. 63, the nominal diagonal element weight w_i assigned to the ith effector was selected using its rate limit RL_i as:

$$w_i = \frac{1}{RL_i} \tag{2}$$

The **B** matrix for the inner-loop allocation included only rows corresponding to the rotational dynamics equations. The \bar{B}

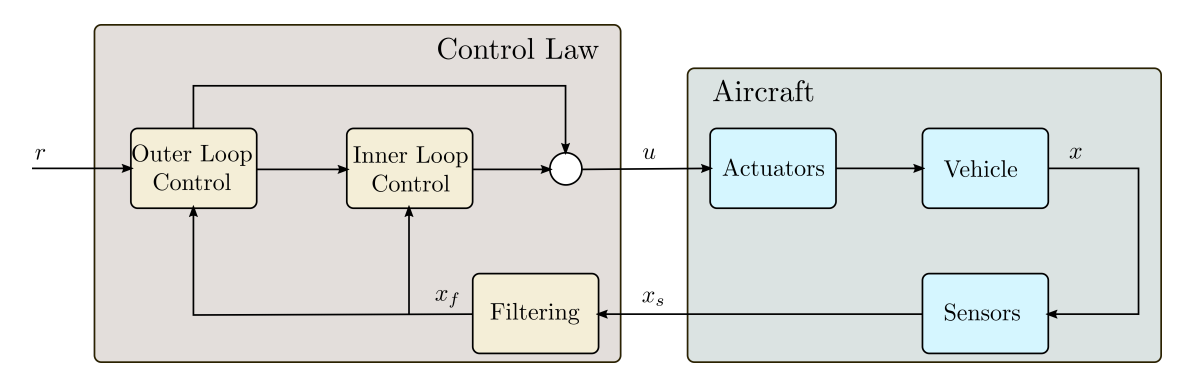


Figure 5: Schematic of the overall RAVEN-SWFT flight control algorithm.

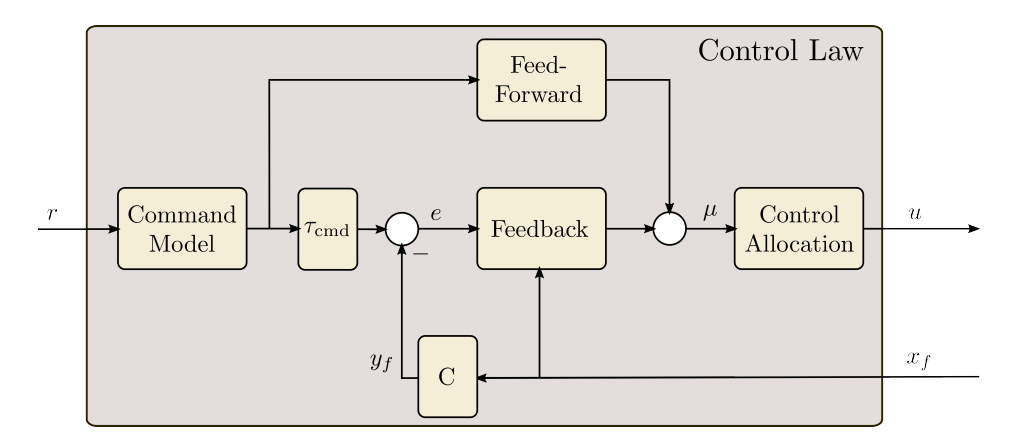


Figure 6: Schematic of the inner- and outer-loop control law structure.

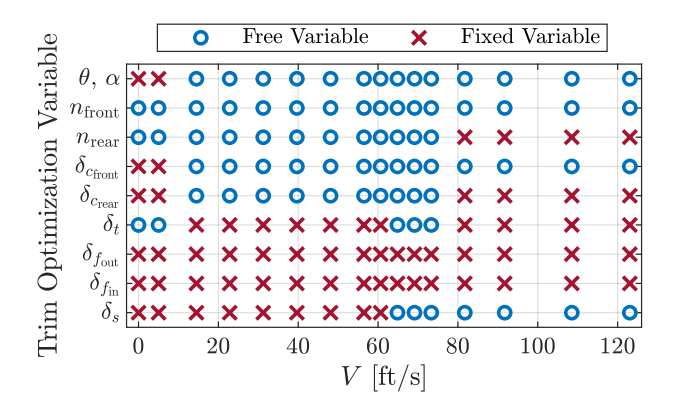


Figure 7: Definition of free and fixed trim optimization variables at each flight condition.

matrix for the outer-loop allocation included rows corresponding to the translational and rotational dynamics equations; however, only the columns of the allocation matrix from the weighted pseudo-inverse solution that correspond to the translational dynamics equations were used for the outer-loop control allocation. The outer-loop allocation also included two additional columns appended to the end of the \bar{B} matrix for the roll and pitch command channels, with weights set as an approximation of the rate limit for roll and pitch attitude commands.

Initial simulations using the conventional weighted pseudoinverse control allocation strategy revealed practical deficiencies, including effectors that have a secondary effect on an axis being over used, sharp changes in the allocation between control design points across the envelope, and adverse interaxis coupling. Modifications to the standard weighted-pseudo inverse allocation solution were implemented to improve the overall allocation strategy. One modification was to set the elements of the \bar{B} matrix that did not contribute the the dominant control effects for the particular axis to zero. Additionally, certain nominal weights w_i at different control design points were multiplied by a scale factor that was adjusted using a constrained nonlinear optimization algorithm with a cost function designed to minimize the variation in each element of the allocation matrix between control design points. Both of these modifications result in a more practical allocation solution, improving the overall flight controller performance. Investigating alternative control allocation strategies using linear or quadratic programming (Ref. 64) or cascading generalized inverse (Ref. 65) allocation methods is a planned area of future research.

Flight Control Law Design

As mentioned previously, the RAVEN-SWFT FCS utilizes nested inner- and outer-loop flight control laws, shown in Figs. 5-6, to control the rotational and translational motion of the aircraft, respectively. The inner- and outer-loop flight control laws each implement a model-following control approach with LQI feedback and a static feedforward inverse

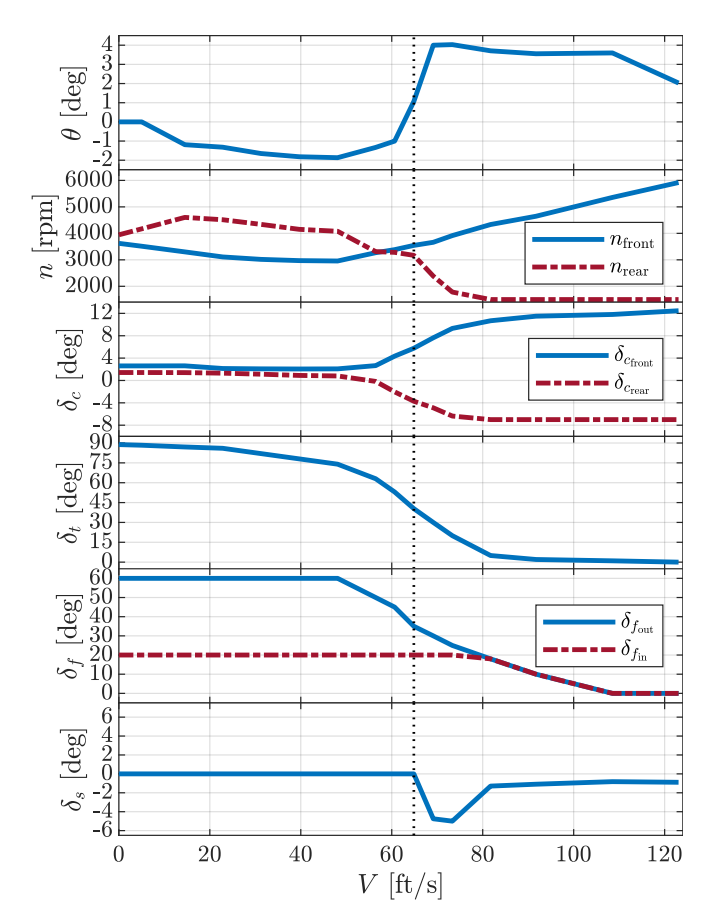


Figure 8: Variation of RAVEN-SWFT trim settings with freestream airspeed.

model approximation.

LQI Feedback Design To design the LQI feedback gains, linear models were obtained from the nonlinear simulation at each of the trim conditions. The linear models were then decomposed into 4-state longitudinal (u, w, q, θ) and lateral-directional (v, p, r, ϕ) systems, where the velocity states can be defined in either the body frame (u, v, w) or heading frame $(\bar{u}, \bar{v}, \bar{w})$ (Refs. 19, 20). The linear systems are then of the form

$$\dot{\mathbf{x}} = \mathbf{A}\mathbf{x} + \mathbf{B}\mathbf{u} \tag{3}$$

$$\mathbf{v} = \mathbf{C}\mathbf{x} \tag{4}$$

Then, defining e = y - r, the augmented system

$$\dot{\boldsymbol{x}}_a = \boldsymbol{A}_a \boldsymbol{x}_a + \boldsymbol{B}_a \boldsymbol{u} + \boldsymbol{B}_r \boldsymbol{r} \tag{5}$$

$$\mathbf{v} = \mathbf{C}_a \mathbf{x}_a \tag{6}$$

can be used for the LQI design, where

$$A_a = \begin{bmatrix} \mathbf{0} & C \\ \mathbf{0} & A \end{bmatrix}, \quad B_a = \begin{bmatrix} \mathbf{0} \\ B \end{bmatrix}, \quad B_r = \begin{bmatrix} -\mathbb{I} \\ \mathbf{0} \end{bmatrix}, \quad C_a = \begin{bmatrix} \mathbf{0} & C \end{bmatrix}$$

Letting $u = -Kx_a$, the optimal feedback gain, K, is computed from the solution, P, to the algebraic Ricatti equation

$$\mathbf{P}\mathbf{A}_{a} + \mathbf{A}_{e}^{\mathsf{T}}\mathbf{P} - \mathbf{P}\mathbf{B}_{a}\mathbf{R}^{-1}\mathbf{B}_{a}^{\mathsf{T}}\mathbf{P} + \mathbf{Q} = \mathbf{0}$$
 (7)

that arises from the solution to the minimization of the quadratic performance index

$$J = \int_0^\infty \boldsymbol{x}_a^{\mathsf{T}} \boldsymbol{Q} \boldsymbol{x}_a + \boldsymbol{u}^{\mathsf{T}} \boldsymbol{R} \boldsymbol{u}$$
 (8)

where $Q \ge 0$ and R > 0. The optimal feedback gain is then

$$\boldsymbol{K} = \boldsymbol{R}^{-1} \boldsymbol{B}_{a}^{\mathsf{T}} \boldsymbol{P} \tag{9}$$

which can be divided into integral and state feedback gain as

$$\mathbf{K} = \begin{bmatrix} \mathbf{K}_i & \mathbf{K}_x \end{bmatrix} \tag{10}$$

Defining q_{ii} as the diagonal elements of Q, tuning was accomplished via a line search over the elements corresponding to the integral states at each trim point, with manual tuning of the elements corresponding to the system states. The input matrix weight was set as $R = \mathbb{I}$ for all trim points. The full 4-state models were used for the design of the inner-loop control law, with pitch attitude tracking in the longitudinal channel and bank angle and yaw rate (defined in either the body or heading frame) in the lateral-directional channel. The outer-loop design also uses the 4-state linear models, where the velocity states can be defined in either the body frame or heading frame, with heading frame longitudinal and vertical speed command tracking in the longitudinal channel and lateral speed tracking in the lateral channel.

The longitudinal and lateral-directional control laws in both the inner and outer loops have an identical structure, depicted in Fig. 6. The outer-loop control law allocation sends commands to the aircraft actuators and to the input of the innerloop, which can be used to specify desired behaviors (e.g., coordinated turns in response to a heading change command).

Command Model and Inverse Model Design The command model defines the desired response of the system to an input command and is specified based on response type. The inner-loop control law uses a second-order response type for all channels defined by

$$\frac{y_{\text{CM}}}{r} = \frac{\omega_n^2}{s^2 + 2\zeta \omega_n + \omega_n^2} \tag{11}$$

while the outer-loop control law implemented a first-order response type:

$$\frac{y_{\rm CM}}{r} = \frac{\omega}{s + \omega} \tag{12}$$

The design of the command models accounted for desired open-loop rise time, settling time, and actuator rates and deflections for a nominal input command. A static approximation of the open-loop inverse dynamics is computed to provide a feedforward command that ensures the open-loop aircraft response matches the command model response. Following the approach in Ref. 66, a low-order equivalent system is fit to the open-loop response (with stabilizing state feedback $u = -K_x x$) of the form

$$\frac{y}{\mu} = \frac{K_{\text{inv}}\omega_{\text{inv}}^2 e^{-\tau_{\text{inv}}s}}{s^2 + 2\zeta_{\text{inv}}\omega_{\text{inv}}s + \omega_{\text{inv}}^2}$$
(13)

for the second-order command model and

$$\frac{y}{\mu} = \frac{K_{\text{inv}}\omega_{\text{inv}}e^{-\tau_{\text{inv}}s}}{s + \omega_{\text{inv}}}$$
(14)

for the first-order command model. Then, the feedforward command term is defined as

$$u_{\rm ff} = K_{\rm ff}r + K_{p_{\rm CM}}y_{\rm CM} + K_{d_{\rm CM}}\dot{y}_{\rm CM} \tag{15}$$

where y_{CM} is the output of the command model and \dot{y}_{CM} is the time derivative of the command model output. For the second-order command model:

$$\begin{split} K_{\rm ff} &= \omega_n^2/(K_{\rm inv}\omega_{\rm inv}^2) \\ K_{P_{\rm CM}} &= (\omega_{\rm inv}^2 - \omega_n^2)/(K_{\rm inv}\omega_{\rm inv}^2) \\ K_{d_{\rm CM}} &= (2\zeta_{\rm inv}\omega_{\rm inv} - 2\zeta\omega_n)/(K_{\rm inv}\omega_{\rm inv}^2) \end{split}$$

For the first-order command model:

$$K_{\rm ff} = \omega/(K_{\rm inv}\omega_{\rm inv})$$

$$K_{p_{\rm CM}} = (\omega_{\rm inv} - \omega)/(K_{\rm inv}\omega_{\rm inv})$$

$$K_{d_{\rm CM}} = 0$$

The time delay $\tau_{cmd} = \tau_{inv}$ is used to delay the reference command to the LQI input, as used in Ref. 66 and shown in Fig. 6. Computing the feedforward gains in this manner provides a static-gain approximation of an inverse model of the dynamics for each channel, resulting in simpler design and implementation than using a transfer function approximation for the inverse model with comparable performance. The command models are implemented in the flight controller as state-space systems, so that the command model derivative, \dot{y}_{CM} is directly accessible without numeric differentiation.

Tuning Approach Control system tuning was performed in a sequential and iterative manner. The inner-loop tuning process starts from the control allocation and works outwards to the LQI control law, command model and feedforward element. Then, the outer-loop tuning progress proceeds similarly through the control allocation, LQI control law, command model, and feedforward element.

Control performance and robustness analyses were performed using both the linearized and nonlinear flight dynamics models. Control law synthesis accounted for closed-loop performance including rise time, settling time, and response overshoot/undershoot; crossover frequency; actuator usage (magnitude and rates); and gain and time-delay margins at the plant input in the nonlinear dynamics simulation.

Gain Scheduling Control law gains, control allocation, trim settings, and other FCS parameters, are scheduled with nominal nacelle tilt angle. The commanded nacelle tilt angle is scheduled with commanded heading-frame forward velocity and is determined in flight by a rate-limited forward velocity command. This approach was chosen over more conventional direct airspeed scheduling since forward velocity is a command variable. Scheduling on a vehicle state that is also a

command variable violates the time-scale separation assumption and introduces undesired coupling between the scheduled state and the control system, precluding the use of measured forward velocity as a scheduling variable. The gain scheduling approach chosen for RAVEN-SWFT allows for a full-envelope flight controller that transitions the aircraft between hover and forward flight conditions.

Feedback Filters VTOL vehicles generally experience significant vibrations due to the proprotor rotation and excited structural resonance. To reduce high-frequency vibrations from propagating into the feedback signals, a series of low-pass and notch filters were placed on the feedback signals upstream of the feedback control laws. The filter parameters were set based on flight data and were designed to sufficiently attenuate undesired high-frequency content while also minimizing the delay added to the feedback signals by the filters.

Flight Control Modes

The RAVEN-SWFT FCS includes three separate FCS modes: FCS Mode 0, FCS Mode 1, and FCS Mode 2. Mode 0 includes inner-loop attitude stabilization and direct thrust commands to the propulsors; Mode 0 is only intended for hover and primarily exists to reduce risk in initial flight testing. Mode 1 includes inner-loop attitude stabilization with an outer-loop altitude rate controller. Mode 2 is a full unified-velocity controller with an attitude-control inner loop and a velocity-control outer loop; Mode 2 includes the highest amount of augmentation and reflects a simplified vehicle operations approach that has parallels to pilot command approaches pursued for passenger-carrying eVTOL aircraft designs (Ref. 67).

The pilot RC transmitter command variables change based on the FCS mode, and are summarized in Table 1. In Mode 0 and Mode 1, the right stick commands pitch and roll attitude, whereas in Mode 2 the right stick commands heading-frame forward and lateral velocity changes. Side-to-side left stick movement commands heading-frame yaw rate in each control mode. Up-down left stick movement commands thrust changes in Mode 0, whereas it commands vertical velocity in Mode 1 and Mode 2. In each FCS mode, the left slider commands the forward velocity setting from zero to the maximum specified forward velocity, which results in nacelle tilt angle changes to transition the aircraft.

Takeoff and Landing Sequence

Key phases of flight for an eVTOL vehicle include its hovering takeoff and landing. The piloted takeoff sequence was given particular focus for the first phase of RAVEN-SWFT flight testing. The pilot uses switches and sticks on the RC transmitter to execute the takeoff sequence. The takeoff sequence follows a list of pre-flight checklist items to ensure personnel and vehicle safety. The current piloted takeoff sequence, from the flight control perspective, is as follows:

Table 1: Pilot command	variable definitions	for each RAVE	N-SWFT fligh	t control mode

Pilot	Command	Mode 0	Mode 1	Mode 2
Interface	Type	(Direct Thrust)	(Vertical Velocity)	(Unified Velocity)
Right Stick (↔)	Lateral	Roll Attitude (ϕ)	Roll Attitude (ϕ)	Lateral Velocity (\bar{v})
Right Stick (1)	Longitudinal	Pitch Attitude ($\Delta\theta$)	Pitch Attitude ($\Delta\theta$)	Forward Velocity $(\Delta \bar{u})$
Left Stick (\leftrightarrow)	Directional	Yaw Rate $(\dot{\psi})$	Yaw Rate $(\dot{\psi})$	Yaw Rate $(\dot{\psi})$
Left Stick (↑)	Vertical	Thrust (ΔT)	Vertical Velocity (\bar{w})	Vertical Velocity (\bar{w})
Left Slider	Transition	Forward Velocity (\bar{u})	Forward Velocity (\bar{u})	Forward Velocity (\bar{u})

- 1. Ensure that the two arm switches are in the upward "disarm" (0) position.
- Select the desired flight control mode using the FCS Mode switch on the RC transmitter.
- 3. While holding the vertical stick command to its negative limit (full downward left stick), move one of the arm switches to the center "arm" (1) position, and then release the self-centering vertical stick. This will arm the vehicle in QGroundControl and allow the the pilot to move all of the control effectors. The proprotor speed will remain at zero for this step.
- 4. Deflect each of the control sticks and visually ensure that each of the 18 servos are active and properly commanding control effector position.
- 5. Move the second arm switch to the center "arm" (1) position (i.e., place both arm switches in the center position). The servos will deflect their corresponding control effector to the trim hover setting. Then, after a brief delay to allow the servos to reach their hover positions, the proprotors will start spinning at the minimum rotational speed setting. Visually ensure that each of the proprotors is spinning.
- 6. Move both arm switches to the downward "engage" (2) position. Then, move the vertical stick down to its most negative position. This will engage FCS Mode 0 at the minimum thrust setting with the integrators disabled to prevent integrator windup.
- 7. Carefully move the vertical stick towards the center position, which will increase the proprotor speed and collective pitch angle towards the trimmed hover thrust settings. The vehicle will elevate above the ground near the center vertical stick position.
- 8. Once the vehicle's distance above ground level surpasses a predefined small separation distance from the ground, as sensed by a LiDAR distance sensor, the FCS will switch into the desired flight control mode set above and enable the integrators in the control laws. This completes the takeoff sequence and the pilot can then execute the flight mission designated for the particular flight.

The current piloted landing sequence is simply to guide the vehicle to a gentle landing and then promptly move both arm switches to the upward "disarm" (0) position, which will set the proprotor speed commands to zero. The pilot can then proceed through the takeoff sequence again to perform another takeoff. An additional automated landing sequence has been successfully tested that uses the LiDAR distance sensor

to determine when the vehicle has landed and automatically disarms the vehicle. Increasing the takeoff and landing automation, as well as the automated flight missions using the RAVEN-SWFT custom flight control software, is planned for future flight control upgrades.

PROGRAMMED TEST INPUTS

One key feature of the custom RAVEN-SWFT FCS is a programmed test input (PTI) injection capability used for system identification. The PTI excitations are summed with the reference command and control effector signals, before and after the flight control laws, as shown in Fig. 9. The automated input types included multistep (Refs. 54,68), frequency sweep (Refs. 54, 69), and multisine excitations (Ref. 54), which were created using the System IDentification Programs for AirCraft (SIDPAC) software toolbox (Ref. 70).

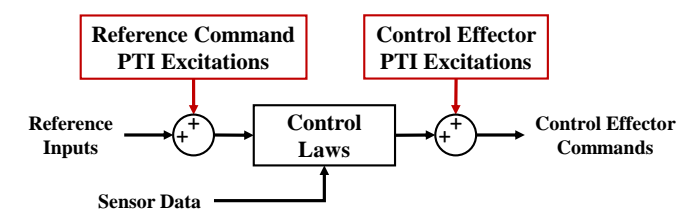


Figure 9: PTI injections relative to the control laws.

Square wave multistep inputs (e.g., doublet, 1-2-1, and 3-2-1-1 inputs) and frequency sweep inputs are injected into the reference command PTIs upstream of the control laws. Currently, doublet (1-1) commands are used to evaluate the control system tracking performance and serve as system identification validation maneuvers. Frequency sweep and the more complex multistep inputs have been exercised for verification purposes, but are not currently planned to be used in the RAVEN-SWFT flight testing. Multisine inputs, described next, are the preferred input type for efficient open-loop model identification for the present application due to the large number of control effectors and aero-propulsive complexity associated with eVTOL vehicles.

Orthogonal phase-optimized multisine inputs (Refs. 54, 71–73) are the primary PTI type used for system identification for the RAVEN-SWFT aircraft. A multisine input is defined as a sum of multiple sinusoidal functions with different amplitudes, frequencies, and phase angles, where the frequencies are chosen to encompass the frequency range corresponding to the system dynamics of interest. To make all

inputs orthogonal in both the time domain and frequency domain, the multisine signal for the jth control effector is assigned sinusoids with a unique subset K_j of discrete harmonic frequency indices selected from the complete set of K available frequency indices. The available frequencies are $f_k = k/T$, k = 1, 2, ..., K, where T is the fundamental period and K/T is the highest excitation frequency. For m total control effectors, the jth input signal $u_j(t)$ is defined as

$$u_j(t) = \sum_{k \in K_j} A_j \sqrt{P_k} \sin\left(\frac{2\pi kt}{T} + \phi_k\right), \quad j = 1, 2, ..., m$$
 (16)

where A_j is the signal amplitude, P_k is the kth power fraction (with $\sum_{k \in K_j} P_k = 1$), ϕ_k is the kth phase angle defined on the interval $(-\pi, +\pi]$, and t is the elapsed time. The phase angles are optimized to obtain a minimum relative peak factor, thereby helping to keep the system close to its nominal flight trajectory while also retaining the same high input energy as a signal without optimized phase angles. Because multiple inputs and all aircraft dynamics of interest are simultaneously excited, the use of multisine inputs allows execution of highly efficient and informative flight testing. A single multisine maneuver can be used to develop a comprehensive aircraft dynamic model around a nominal flight condition, including nonlinear aerodynamic phenomena and control interaction effects.

For RAVEN-SWFT flight testing, individual multisine signals were generated for each of the 24 independent control effectors. Additionally, multisine signals were created for the reference commands $(\eta_{lon}, \eta_{lat}, \eta_{dir}, \eta_{ver})$ tracked by the control system to provide additional state perturbations supplementing state disturbances resulting from control effector PTI injections. In previous RAVEN-SWFT 3DOF wind-tunnel testing, the multisine directional reference commands were noted to be particularly helpful for improving the parameter estimate values associated with lateral speed v and yaw rate r (Ref. 16). Combining the control effector and reference command multisine signals, which are all executed simultaneously, there are a total of 28 independent excitation signals. The RAVEN-SWFT flight-test multisine design has some minor differences compared to the 27 component RAVEN-SWFT multisine design described in Ref. 16 that was used for RAVEN-SWFT 3DOF wind-tunnel testing.

To create the RAVEN-SWFT multisine signals used for flight testing, several harmonic components were assigned to each multisine signal, where the overall frequency range was set to between 0.05 Hz and 1.75 Hz in accordance with frequencies where the rigid-body dynamics were predicted to manifest. The harmonic components for the reference commands and slower moving control effectors were selected to be consistent with the approximate bandwidth of each signal. The collective pitch, outboard tilt, stabilator, flaperon, and rudder multisine signal harmonic components spanned the full frequency range and were each assigned 18 frequency components. The proprotor rotational speed, inboard tilt, and attitude command harmonic components were focused into lower frequencies due to their lower bandwidth and contained 16,

12, and 5 frequency components, respectively. The frequency components were assigned to each signal in an alternating manner and were distributed to avoid neighboring control effectors having neighboring frequency components, similar to the approach described in Ref. 74.

The input spectra for the final set of RAVEN-SWFT flight-test orthogonal phase-optimized multisine signals is shown in Fig. 10. There are 428 total harmonic components with a fundamental period of T=260 seconds. The overall frequency range is between $f_{\rm min}=0.05$ Hz and $f_{\rm max}=1.754$ Hz with a frequency resolution of $\Delta f=1/T=0.00385$ Hz. Figure 11 shows the first 20 seconds of the input excitation signals with $A_j=1$. For system identification experiments, a gain is applied to scale each input signal to a sufficient amplitude to obtain a good signal-to-noise ratio, while not deviating far from the trimmed flight condition. Note that the nominal RAVEN-SWFT 60-second system identification maneuver length is longer than the 20-second input signal duration shown for demonstration purposes in Fig. 11.

Because the RAVEN-SWFT is unstable over a significant portion of its flight envelope, the feedback control system must be active when operating the aircraft. Therefore, the control effector signals sent to the motors and actuators in flight testing are different than the designed signals shown in Fig. 11 and become somewhat correlated due to distortion from the active FCS; however even with this distortion and diminished orthogonality, the modeling variables are generally sufficiently decorrelated for model identification because the control effector excitation inputs are added downstream of the flight control laws (Refs. 54, 73). An active control system may still slightly degrade modeling results, as compared to modeling a vehicle that does not require a control system to be active while executing system identification maneuvers, but the adverse effects of the FCS on the system identification experiment are largely mitigated by following this approach.

To execute an automated RAVEN-SWFT system identification maneuver, starting from a trimmed flight condition, the pilot reverses the polarity of a PTI slider on the RC transmitter to enable the PTI excitations. The vehicle FCS then injects the selected PTI into the control effector and/or reference commands, perturbing the vehicle around its reference conditions without requiring any additional pilot inputs. After completing the maneuver, the pilot returns the PTI slider to its original position to disable the PTI excitations.

The form of the PTI injected by the FCS is governed by multiple RC transmitter channels. The "PTI Type" (multisine, frequency sweep, or multistep) is set using a three position switch on the RC transmitter. The "PTI Option" for each PTI Type is then able to be selected using a combination of two additional three position switches, called the "PTI Mode" and "PTI Submode" as:

$$[PTI Option] = 3 \times [PTI Mode] + [PTI Submode]$$

Table 2 lists the current PTI Option settings for each PTI Type, where there is room for future expansion up to 9 options for each PTI Type.

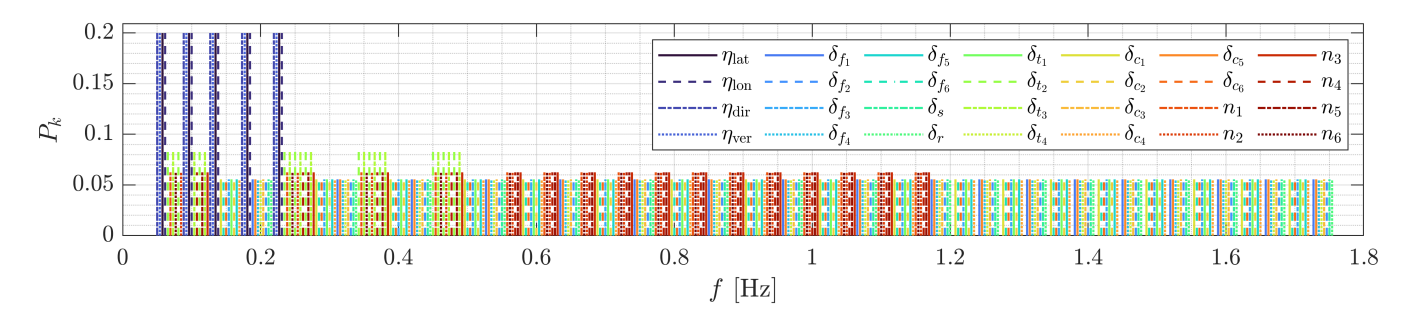


Figure 10: RAVEN-SWFT flight-test multisine input spectra for each reference command and control effector.

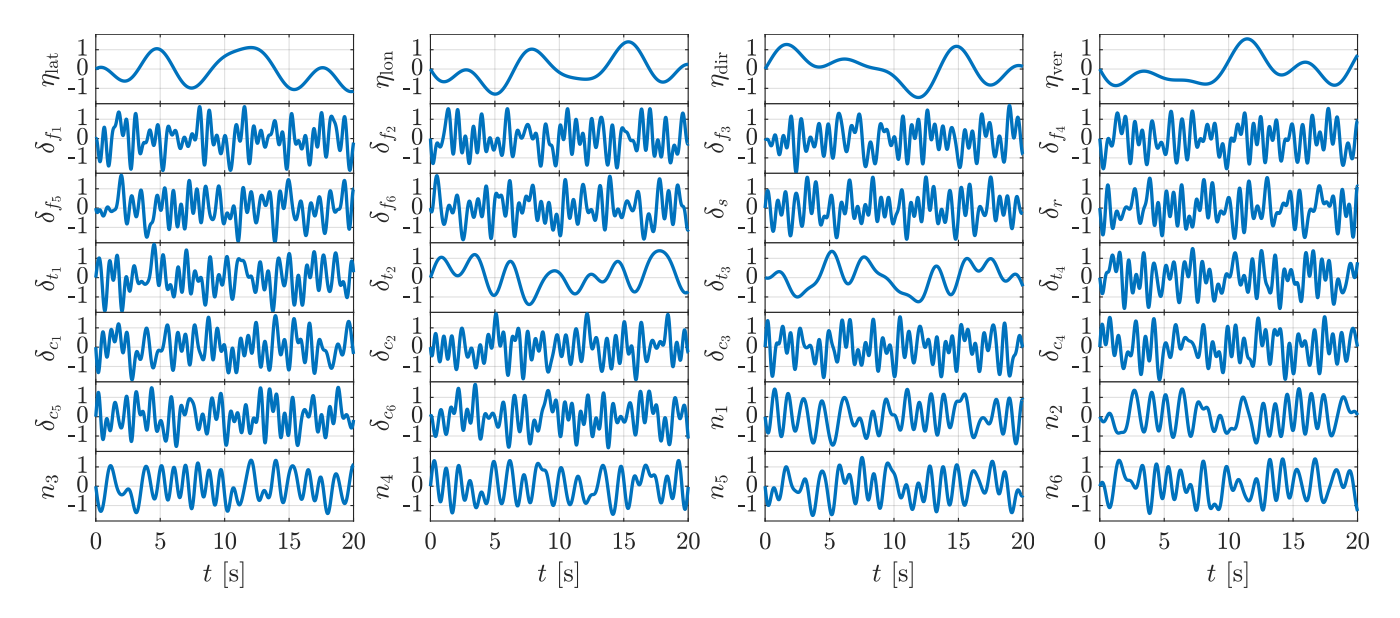


Figure 11: Normalized RAVEN-SWFT multisine input signal for each reference command and control effector.

Table 2: RAVEN-SWFT PTI option descriptions

	PTI	
PTI Type	Option	PTI Functionality
Multisine	0	Control Effector (CE) Multisine
	1	Reference Cmd. (RC) Multisine
	2	Combined CE and RC Multisine
Frequency	0	Lateral Command Sweep
Sweep	1	Longitudinal Command Sweep
	2	Directional Command Sweep
	3	Vertical Command Sweep
Multistep	0	Lateral Command Steps
	1	Longitudinal Command Steps
	2	Directional Command Steps
	3	Vertical Command Steps

To achieve an appropriate amount of vehicle excitation, the overall PTI amplitude is scaled using a rotary knob on the RC transmitter. Furthermore, the individual command multistep/frequency sweep amplitude, as well as the multisine amplitude for groups of similar control effectors (e.g., outboard flaperons, inboard flaperons, front collective, rear collective, etc.) and each reference command, can be scaled separately by modifying parameters on a GCS computer. Additionally, for

multistep inputs, the square wave step type (e.g., 1-1, 1-2-1, 3-2-1-1) and step time interval can be adjusted using parameters set on the GCS. The current RC transmitter interface and GCS PTI parameters are discussed further in the next section.

CONTROL SYSTEM INTEGRATION

In parallel to simulation-based RAVEN-SWFT FCS development, efforts were undertaken to identify a streamlined solution to deploy a custom Simulink® model onto flight vehicle hardware. Through the use of low-cost surrogate vehicles, a process to deploy custom flight control logic developed in Simulink® onto a Pixhawk flight computer was identified and refined (Refs. 51, 75, 76). The flight controller deployment process, which uses the MathWorks® UAV Toolbox and its Support Package for PX4 Autopilots (Ref. 49), was determined to be a suitable solution for RAVEN-SWFT with a few vehicle hardware-related modifications. The default PX4 outer- and inner-loop control laws are replaced by the custom RAVEN-SWFT control laws described above, but the flight controller deployed onto the Pixhawk retains most of the other functionality in the PX4 Autopilot firmware, such as the state estimation algorithm, input/output drivers, safety logic, and data logging capabilities. These methods allow for rapid deployment of a custom flight control algorithm, where a new control software update can be built and deployed onto the Pixhawk flight computer in under five minutes.

After the RAVEN-SWFT FCS was designed and tested in simulation, steps were taken to integrate the control logic onto the vehicle hardware. Initially, simulations were executed with the Simulink® model running on a laptop computer and communicating with the vehicle sensors, control effectors, and RC transmitter/receiver. Then, the Simulink® model was autocoded onto a Pixhawk flight computer to execute experimental testing. The top level of the flight control software Simulink® diagram used for integration onto the RAVEN-SWFT vehicle is shown in Fig. 12, which includes the inputs from the vehicle, flight control system, and outputs to the vehicle. The overall structure is similar to the simulation structure shown in Fig. 4, except that the FCS Input and FCS Output subsystems in Fig. 12 are used to interface with the vehicle and the vehicle model is replaced by the actual vehicle dynamics. The Flight Control System subsystem is identical to the equivalent subsystem shown in Fig. 4; the subsystem contains the RAVEN-SWFT control algorithm and the PTI injection capabilities described previously, as well as other logic necessary to safely fly the vehicle.

The following subsections describe the implementation of the FCS onto RAVEN-SWFT hardware. The RAVEN-SWFT FCS described in this work was created and deployed using MATLAB/Simulink[®] R2024a (Ref. 49) and PX4 Version 1.14 (Ref. 77).



Figure 12: Top-level view of the flight control software Simulink[®] diagram integrated onto the vehicle.

Flight Control System Inputs

The FCS Inputs subsystem includes functionality to read sensor and state estimate data, read RC transmitter inputs, read GCS commands, and maintain an internal FCS elapsed time counter.

Vehicle Data Pertinent signals are read from the PX4 micro object request broker (uORB) communication system (Ref. 78) using the UAV Toolbox "PX4 uORB Read" Simulink® block. The signals read into the RAVEN-SWFT FCS include:

- · Vehicle attitude in quaternions
- · Body-axis angular velocity
- Inertial velocity
- · Latitude, longitude, and altitude
- · True airspeed
- · Estimated wind

- Proprotor rotational speed
- Above ground distance

The vehicle attitude, angular velocity, and inertial velocity are estimated states obtained from either the PX4 state estimation algorithm or an external inertial navigation system (INS). The external INS was found to improve FCS performance and is the default state estimation source for RAVEN-SWFT. Inertial position and winds are from the PX4 state estimator. True airspeed, proprotor rotational speed, and above ground distance are from an external airspeed sensor, the proprotor ESCs, and an external LiDAR sensor, respectively.

RC Transmitter An RC transmitter capable of commanding 16 independent channels is used as the pilot interface to command the vehicle trajectory and execute various research functionality. The channels are composed of signals from the left and right stick position (4 channels), left and right sliders (2 channels), left and right rotary knobs (2 channels), and 8 discrete switches (8 channels) including a two-position locking switch and 7 three-position switches. Both of the pilot control sticks are self centering due to the hands-off state-hold nature of the primary FCS modes (Modes 1 and 2). The assignments of each transmitter channel to the corresponding FCS response are summarized in Table 3. Additionally, Fig. 13 shows a schematic of the transmitter layout annotated with the designated interface functionality. This transmitter configuration builds on transmitter setup approaches discussed in Refs. 76 and 79 to meet the research requirements for the RAVEN-SWFT vehicle testing.

Table 3: RAVEN-SWFT RC transmitter channel descriptions for system identification flight testing

Label	Switch Type	FCS Functionality
P1	Right Stick (\leftrightarrow)	Lateral Command
P2	Right Stick (1)	Longitudinal Command
P3	Left Stick (\leftrightarrow)	Directional Command
P4	Left Stick (\$)	Vertical Command
P5	Right Slider	Enable/Disable PTI
P6	Left Slider	Transition (\bar{u}) Command
P7	Right Knob	Overall PTI Amplitude
P8	Left Knob	Miscellaneous Testing
SA	3-Position	FCS Gain Adjustment
SB	Locking	Flight Termination
SC	3-Position	FCS Mode
SD	3-Position	Arm/Engage Switch 1
SE	3-Position	Arm/Engage Switch 2
SF	3-Position	PTI Type
SG	3-Position	PTI Mode
SH	3-Position	PTI Submode

The RC transmitter sticks command the lateral, longitudinal, directional, and vertical vehicle response based on the flight control mode (see Table 1). The flight control research commands are located on the left side of the transmitter, which includes the FCS mode switch, a switch to enable FCS gain scaling functionality, the transition forward velocity command on

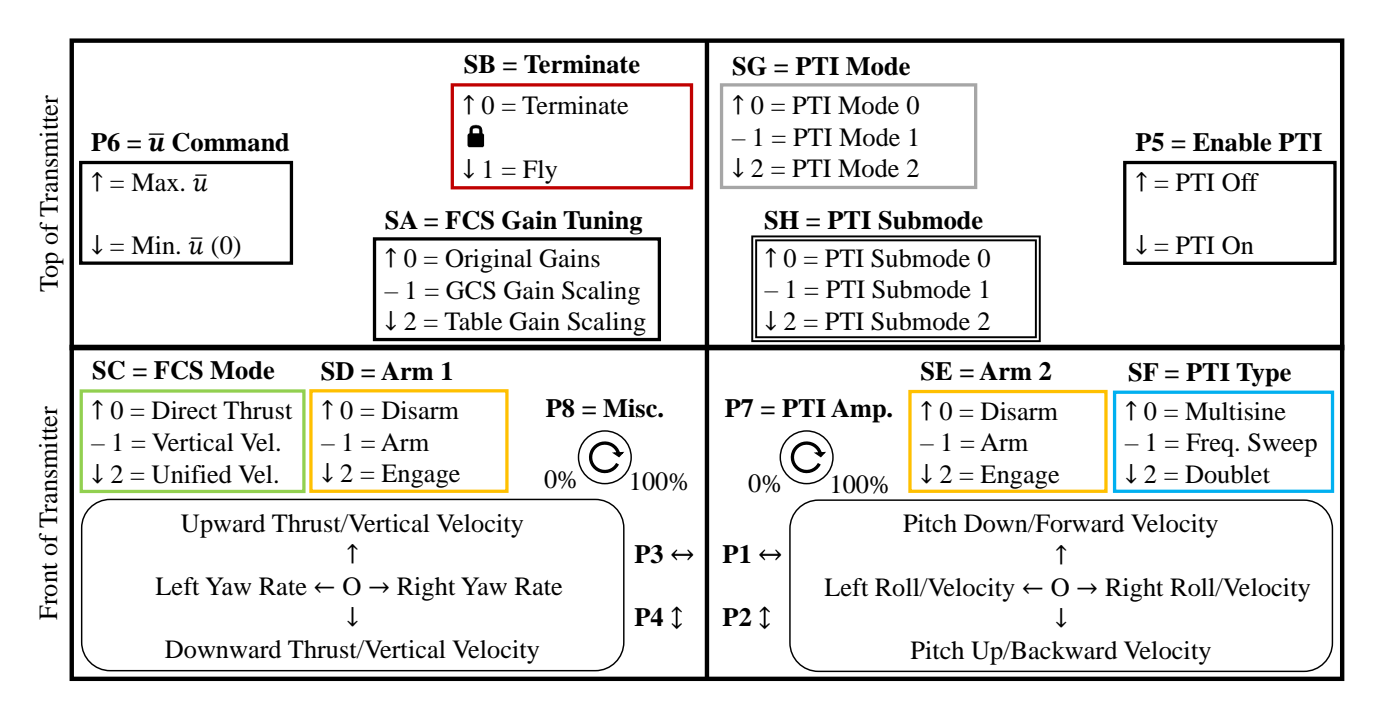


Figure 13: RAVEN-SWFT RC transmitter programming for modeling and controls research.

a slider, and a locking flight termination switch. The left rotary knob is used to execute miscellaneous FCS tests (for example, the knob was temporarily programmed to initiate an automatic landing command in initial flight testing). The system identification research commands are located on the right side of the transmitter and include a slider to enable/disable PTIs, a PTI Type switch, a PTI Mode switch, a PTI Submode switch, and a rotary knob assigned to adjust the overall PTI amplitude. Furthermore, the two centermost switches on the left and right side of the RC transmitter are used together to initiate the vehicle startup and shutdown sequence. Two switches are dedicated to this purpose to require two deliberate actions by the pilot to initiate the arming sequence (thereby, substantially reducing the likelihood of accidentally tripping this critical functionality). Similarly, the locking flight termination switch requires two deliberate actions (lifting the switch and then changing its position) to initiate flight termination.

In addition to the 16 RC channels, an additional PX4 parameter is read to monitor the RC transmitter link and, if necessary, initiate the vehicle lost-link response. The lost-link response, as well as other flight authorization features will be discussed in the next section. The RC channels and transmitter link signals are each read into the FCS using the UAV Toolbox "PX4 uORB Read" Simulink® block.

Ground Control Station Parameters Following the method described in Ref. 51, custom GCS parameters were created to adjust numerous flight control and system identification parameters within the custom FCS on the GCS computer. The custom flight control parameters included:

• Pilot stick sensitivity for reference commands (9 parameters)

- A toggle between internal PX4 and external INS state estimates (1 parameter)
- Distance sensor weight-on-wheels thresholds (2 parameters)
- Feedback filter settings (5 parameters)
- Servo-actuator calibration ground testing commands (4 parameters)
- Flight control gain scaling values (15 parameters)
- Forward velocity and acceleration limits (4 parameters)
- Nacelle tilt command rate limits (2 parameters)

The custom system identification parameters included:

- Lateral, longitudinal, directional, and vertical reference command multisine PTI amplitude (4 parameters)
- Outboard flaperon, inboard flaperon, stabilator, rudder, outboard nacelle tilt, inboard nacelle tilt, front collective, rear collective, front motor rotational speed, and rear motor rotational speed multisine PTI amplitude (10 parameters)
- Lateral, longitudinal, directional, and vertical reference command multistep and frequency sweep PTI amplitude (4 parameters)
- Lateral, longitudinal, directional, and vertical reference command multistep PTI step time interval (4 parameters)
- Square wave multistep PTI waveform: doublet (1-1), 1-2-1, or 3-2-1-1 (1 parameter)

The GCS commands are individually read into the FCS using the UAV Toolbox "PX4 Parameter Read" Simulink[®] block. For safety considerations, the GCS parameters are only adjusted in QGroundControl (Ref. 80) while the vehicle is disarmed on the ground; whereas, the RC transmitter is used to command the vehicle and execute/adjust research functionality in real time while flying the vehicle.

Flight Control System Outputs

The FCS Outputs subsystem sends commands to the control effectors, transmits data to the GCS, and logs internal flight control signals.

Control Effector Commands The DroneCAN communication protocol (Ref. 81) is used for the communication with ESCs and control surface servo-actuators. Motor speed and control deflection commands from the FCS are converted to DroneCAN messages that are sent to the vehicle using the ActuatorMotors and ActuatorServos uORB topics accessed through the UAV Toolbox "PX4 uORB Write" Simulink® block. To accommodate the large number of control effectors present in eVTOL vehicle designs, a custom version of PX4 was created that included several modifications to allow the use of up to 20 CAN ESCs and 20 CAN servos.

The ESCs are sent commands that are directly related to the rotational speed requested by the flight controller. The servos commands, however, are sent as scaled values between −1 and +1 that corresponds to the programmed minimum and maximum position limits. Because the command to physical deflection is generally a nonlinear relationship, a calibration curve was created and implemented into the FCS for each servo to convert between the physical commanded deflection requested by the FCS and servo commands sent to the servos. The servo calibration is performed using a special ground-based "servo calibration mode" built into the FCS and executed using calibration-specific GCS parameters. A predetermined list of calibration commands in a randomized order are commanded through the GCS; the physical control effector deflections are measured using a digital angle gauge and recorded for each command. A polynomial is then fit to the calibration data to convert between command and physical deflection, which is implemented into the FCS to compute the CAN servo command.

Data Logging Pertinent internal signals from the FCS are logged in the PX4 "ULog" format (Ref. 82) on an SD card using the UAV Toolbox "PX4 ULog" Simulink® block and custom uORB messages created for RAVEN-SWFT. The logged internal signals included RC commands, sensor data, feedback states, control effector commands in engineering and CAN command units, reference commands, and FCS status information. In addition to the internal FCS signals, sensor data, internal PX4 INS and external INS states, and PX4 status messages are stored in the ULog file by specifying these desired topics in the standard PX4 logger topics file.

GCS Data Following the approach described in Ref. 51, signals from the FCS are sent to a research GCS via a telemetry radio. In addition to a standard QGroundControl ground station, the custom research ground control station built in Simulink[®] allows for more tailored displays for the particular aircraft, as well as displays allowing improved monitoring of the flight controller performance and research maneuvers. The research GCS telemetry signals include the vehicle

status, proprotor rotational speed, FCS reference commands, FCS transition commands, control effector engineering commands, sensor measurements and health status, and FCS/PTI modes.

Data Acquisition System

In addition to the sensor, state estimate, and control data logged on the Pixhawk, a Data Acquisition System (DAS) was developed to log data from the ESCs, control surface servo-actuators, batteries, and an air-data probe. The DAS data used for post-test control and system identification analyses include the commanded motor rotational speed, measured motor rotational speed, commanded servo position, actual servo position, and air-data information. Additional data, such as the ESC and servo voltage, current, and temperature, are useful for evaluating vehicle system performance.

SOFTWARE ASSURANCE AND AIRWORTHINESS CONSIDERATIONS

A software assurance process was developed for the custom RAVEN-SWFT FCS to meet software development requirements and ensure safe flight operations, while also retaining agility in the development and modification of research software for a subscale, modest cost vehicle. The RAVEN-SWFT software development framework follows general engineering software best practices including version control, software testing, detailed code documentation, and peer review. The RAVEN-SWFT simulation and FCS software is hosted and version controlled using an internal GitLab repository (Ref. 83). The general process for modifying the software is as follows:

- 1. Create an issue ticket describing the intended changes.
- 2. Create a new branch from the main version of the software remote repository associated with the issue ticket.
- Pull a local version of the new branch to the developer's computer.
- Make the desired changes on a local version of the branch and include detailed comments explaining the updates.
- 5. Perform testing to ensure that the software changes have the desired effect.
- 6. Commit and push the changes to the remote branch of the software repository.
- Create a merge request that includes a detailed description of the software changes.
- 8. Peer review of the software changes is conducted by at least one subject matter expert. The assessment includes reviewing the changes relative to the main version of the repository (e.g., using the visdiff command in MATLAB[®]), as well as performing software unit tests and regression tests.
- If the software changes are deemed to be successful, the software reviewer adds a detailed comment to the GitLab merge request describing the review steps and outcomes.
- 10. The software changes are merged into the main version of the GitLab repository by the software reviewer.

This set of procedures upholds a rigorous software vetting process ensuring safety of flight, while also allowing for flexibility and rapid development of RAVEN-SWFT research software.

From the RAVEN-SWFT flight authorization viewpoint, it is most important to ensure the safety of test personnel and bystanders, protect infrastructure outside of the vehicle, and keep the vehicle on the flight-test range. Therefore, the most important aspects of the FCS software development, integration, and testing is to ensure that these safety requirements are met. The vehicle's integrity is still important and every effort is made to avoid harm to the vehicle; however, this is considered a secondary priority for the RAVEN-SWFT.

A multilayered flight termination system (FTS) is employed to ensure that the personnel, infrastructure, and range containment safety objectives are met. As the first safety mechanism, a flight termination switch was implemented on the RC transmitter that allows the pilot to enable the FTS flight mode at any time. To prevent accidental tripping of this switch, a locking switch was installed on the RC transmitter that requires the pilot to lift and then adjust the switch position to initiate flight termination. A second safety mechanism is a geofence that enables flight termination if horizontal or vertical boundaries are exceeded. The termination geofence acts as an "electronic tether" from the software assurance and flight authorization perspective. For both flight termination actions, the vehicle response is to disable proprotor motor power and set the control surfaces to pro-spin settings. This FTS logic resides within the unmodified portion of the PX4 firmware and is independent of the custom RAVEN-SWFT FCS software that replaces the internal PX4 flight control laws. Nonetheless, to ensure the correct response of this critical functionality, termination initiation is verified on the ground at the start of each flight day and after re-compiling the custom flight software.

Additional RAVEN-SWFT flight safety logic includes a lost-link response and a second geofence inside of the flight termination geofence. Currently, in both scenarios, the programmed response is to automatically return to a hover state and land in place. Contrary to the flight termination functionality, the return-to-hover (RTH) capability resides within the custom RAVEN-SWFT FCS software. For the purpose of flight-test range containment, the RTH response is strongly preferred over the FTS response. Similar to the FTS, the lost-link sequence initiation is verified on the ground at the start of each flight day and after re-compiling the custom flight software. Furthermore, the RTH response was exercised in tethered flights prior to conducting free flight testing.

As a final safety feature, the pilot has the ability in-flight to switch to an emergency "Glider Mode" by moving both arm switches to their center positions. The vehicle will then switch to direct "stick-to-surface" manual control. Here, the lateral, longitudinal, and directional stick positions commands aileron, stabilator, and rudder deflection directly, respectively, with the motors disabled. This mode gives the pilot the ability to quickly bring the vehicle down to the ground while also retaining influence over the vehicle's trajectory, unlike the other

flight safety modes that execute an automated response.

FLIGHT-TEST APPROACH

This section describes the flight-test buildup approach pursued for RAVEN-SWFT from the FCS software development perspective. After simulation development and testing, the vehicle underwent extensive 3DOF testing, followed by tethered and free flight testing. At the time of writing this paper, the RAVEN-SWFT is actively undergoing the initial phases of its flight testing.

3DOF Wind-Tunnel Testing

3DOF free motion wind-tunnel testing was discussed earlier in the paper in the context of aero-propulsive damping characterization for the RAVEN-SWFT vehicle. Although, dynamic derivative identification to improve the RAVEN-SWFT flight dynamics model was an important aspect of the 3DOF wind-tunnel testing, an equally valuable part of the test was focused on evaluation and refinement of the RAVEN-SWFT FCS software.

Flight testing of new experimental FCS software must proceed very cautiously because of the elevated risk posed to the vehicle. Therefore, substantial effort is invested in performing flight simulations and hardware-in-the-loop bench testing before flight testing new FCS software. However, because of differences in the simulation and hardware-in-the-loop environment compared to flight, these software verification efforts can fail to identify possible issues that arise when operating onboard a vehicle in a flight-test environment, which can lead to expensive, unforeseen project delays. 3DOF wind-tunnel testing, alternatively, allows the vehicle to be flown in multiple rotational degrees of freedom in a flight-like environment, while posing little risk to the vehicle, similar to bench testing. The 3DOF wind-tunnel test capability allows the FCS software to be efficiently and rigorously tested, while also permitting rapid implementation and testing of software changes based on observations and data from testing. FCS software verification constituted a major aspect of the RAVEN-SWFT 3DOF wind-tunnel testing, which accelerated FCS software development and served as a substantial risk-reduction effort for subsequent flight testing.

The 3DOF wind-tunnel apparatus introduced previously (see Fig. 3), allows for free simultaneous roll, pitch, and yaw motion where the active control effectors are used to control aircraft rotational motion. Any of the rotation axes can also be fixed for 1DOF or 2DOF testing. The RAVEN-SWFT powered-airframe 3DOF wind-tunnel test started by evaluating the control laws in a single axis with the other control axes disabled and their rotational degrees of freedom locked. Testing then proceeded to include two and three free degrees of freedom. Ultimately, the custom FCS was able to be rigorously tested and refined on the 3DOF test apparatus through the transition envelope using similar hardware and flight control software planned to be used in flight testing. A few of the minor software differences include:

- 1. only the inner-loop attitude-stabilization control laws were able to be tested,
- the pilot stick and FCS reference commands were the roll, pitch, and yaw attitude (the inner-loop 3DOF directional control law used yaw attitude as the feedback variable, whereas the flight-test directional control law uses yaw rate as the feedback variable),
- 3. the transition command was based on the wind-tunnel dynamic pressure setting, and
- 4. the operational logic was simpler because the vehicle was constrained, did not require takeoff/landing capabilities, and the FCS was generally engaged once the windtunnel dynamic pressure for the desired test condition was achieved.

Nonetheless, most of the FCS software was able to be exercised and refined with minimal risk posed to the vehicle in this important intermediate step prior to conducting flight testing. Sufficient inner-loop flight control performance was demonstrated in transition throughout the wind-tunnel test envelope, in addition to hardware integration verification and vehicle component stress testing, building confidence for flight testing.

3DOF Hover Testing

After the 3DOF wind-tunnel testing was completed, focus shifted to completing the FCS software updates necessary for flight testing, which included the outer-loop control laws, takeoff/landing logic, and flight safety logic. Then, efforts shifted to verifying the flight-test software updates again on the same 3DOF test apparatus that was used in wind-tunnel tests, but this time in a large, open flight laboratory setting using the full flight-test software in FCS Mode 0. The 3DOF apparatus and RAVEN-SWFT aircraft were secured to a heavy metal table, as shown in Fig. 14, and testing was conducted primarily indoors at the Autonomy Lab for Intelligent Flight Technology (ALIFT) facility at NASA LaRC. This setup reduced hover proprotor wake recirculation effects compared to the wind-tunnel test section, allowing for improved hover flight control law evaluation (note that this adverse wind-tunnel proprotor wake recirculation effect only occurs in hover, with the tunnel airflow off-the proprotor wake is blown downstream with the tunnel airflow on, which avoids adverse wind-tunnel proprotor wake recirculation effects). In addition to testing the Mode 0 flight control algorithm in hover, the safety features (flight termination response, geofence response, etc.), flight operations logic, and flight-test procedure rehearsals were able to be exercised and refined.

Tethered Flight Testing

After completing the 3DOF testing, the vehicle was reconfigured for flight-test operations and a tether attachment was installed in the center of the wing/fuselage. The tether attachment was designed to run through the center of gravity of the vehicle to avoid imparting adverse moments during testing. Additionally, a small counterweight was installed on the belay to remove slack from the line. Tethered hover testing was



Figure 14: RAVEN-SWFT hover 3DOF test setup.

conducted at Vertiport #2 at the NASA LaRC City Environment Range Testing for Autonomous Integrated Navigation (CERTAIN) flight-test range. The tether was suspended above the vertipad from a large articulating boom lift, as shown in Fig. 15.



Figure 15: RAVEN-SWFT tethered flight-test setup.

The RAVEN-SWFT tethered flight testing was used to verify the utility of each flight control mode in hover, the flight-test PTI injection capabilities, and the takeoff/landing logic prior to conducting free flight testing without the tether. A photo of the RAVEN-SWFT vehicle in flight on the tether is shown in Fig. 16. Although the risks to the vehicle in tethered flight testing are higher compared to 3DOF testing, tether testing offers the ability to more thoroughly test the full capabilities of the hover flight-test FCS algorithm. Also, the vehicle can

often be spared by the tether operator in case of unexpected anomalies that could cause substantial damage to the vehicle during free flight testing. Hence, tether testing offered a helpful opportunity to provide an incremental risk-reduction step between 3DOF and free flight testing.



Figure 16: Tethered RAVEN-SWFT hover flight testing.

Hover Flight Testing

After verifying the hover flight control software in tethered flight testing, the vehicle was detached from the tether and proceeded to hover free flight testing. The hover testing was composed of piloted assessment of the vehicle response, piloted doublets, automated square wave doublets, and automated multisine maneuvers to assess the performance of multiple RAVEN-SWFT flight control modes and to collect system identification flight data enabling validation of the baseline RAVEN-SWFT aero-propulsive model. The RAVEN-SWFT flight-test research started immediately, including enabling the 28 component multisine PTI on the very first free flight of the aircraft. A photo of the RAVEN-SWFT performing free flight testing is shown in Fig. 17. Note that the metal tether connection apparatus was still connected in this photo (without the tether rope connected) to allow for the flexibility of switching between tethered and free flight testing, if desired. The tether connection apparatus will be removed after completing hover and low-speed transition testing.



Figure 17: Initial RAVEN-SWFT hover flight testing.

Transition Flight Testing

The next step in the RAVEN-SWFT flight-test campaign is to gradually expand testing throughout the transition envelope. At the time of submitting this paper, the RAVEN-SWFT transition envelope expansion flight-test campaign has just begun and initial low-speed flights have been completed.

At several conditions throughout the RAVEN-SWFT transition envelope, the flight control performance is planned to be evaluated using piloted and automated doublet maneuvers. Additionally, flight data will be collected using multisine maneuvers to validate and, if necessary, adjust the baseline RAVEN-SWFT transition model. If improved flight control performance is desired at a particular flight condition, the flight control design parameters are planned to be updated using the flight dynamics simulation with aero-propulsive model updates identified from flight testing.

CONCLUDING REMARKS

There are numerous eVTOL aircraft research areas to address prior to bringing these novel vehicles into mainstream operation. The RAVEN-SWFT tiltrotor vehicle has been developed at NASA LaRC to enable advanced eVTOL aircraft modeling and flight controls research. An attribute of the RAVEN project that distinguishes it from similar pursuits in industry is the objective to openly publish methods and data to facilitate collective research advancement helping to enable future AAM transportation methods.

This paper provided an overview of the dynamic modeling and flight control software development activities for the RAVEN-SWFT aircraft. Initially, wind-tunnel testing was conducted to develop a high-fidelity flight dynamics simulation for the aircraft enabling model-based flight control system design. A robust, well-performing, full-envelope flight control algorithm was designed to enable RAVEN-SWFT testing and validation of flight controls research. The flight control algorithm included an extensive programmed test input injection capability used to assess the flight control system performance and enable efficient system identification flight testing. After integrating the flight control software onboard the RAVEN-SWFT vehicle, an incremental flight-test buildup approach was employed, including 3DOF free motion wind-tunnel testing and tethered hover flight testing. At the time of submission of this paper, the RAVEN-SWFT has completed its hover test campaign and has just begun transition envelope expansion flight testing. The RAVEN-SWFT flight testing serves as a means of validating modeling and flight controls research that has previously only been demonstrated in simulation and wind-tunnel testing. The RAVEN-SWFT modeling and flight control software development approach has been successful and similar methods are recommended for future subscale aircraft development programs.

ACKNOWLEDGMENTS

This research was funded by the NASA Aeronautics Research Mission Directorate (ARMD) Transformational Tools

and Technologies (TTT) project and Flight Demonstrations and Capabilities (FDC) project. RAVEN-SWFT vehicle development and testing support was provided by Gregory Howland, Brayden Chamberlain, Jody Miller, David North, Justin Lisee, Neil Coffey, and Collin Duke. Additional wind-tunnel test support was provided by Ronald Busan, Stephen Farrell, Earl Harris, Richard Thorpe, Clinton Duncan, Wes O'Neal, Lee Pollard, Stephen Riddick, and Vincent Spada. The 3DOF test apparatus used in this work was designed and built by Ronald Busan with integration support from personnel in the Flight Dynamics Branch at NASA Langley Research Center. Other members of the RAVEN project who contributed to the RAVEN-SWFT vehicle development, flight control system development, wind-tunnel testing, and flight testing include: Michael Acheson, Jacob Cook, Jacob Schaefer, Tenavi Nakamura-Zimmerer, Siena Whiteside, and Jason Welstead. Discussions with Julia Brault, Ronal George, Ankur Bose, Arun Mathamkode, Devin Cote, and Cameron Bosley from The MathWorks, Inc. under Nonreimbursable Space Act Agreement SAA1-38060 helped to refine the RAVEN-SWFT control system implementation approach. The contributions from all team members are gratefully acknowledged and appreciated.

REFERENCES

- Johnson, W., Silva, C., and Solis, E., "Concept Vehicles for VTOL Air Taxi Operations," AHS Technical Conference on Aeromechanics Design for Transformative Vertical Flight, January 2018.
- Silva, C., Johnson, W., Patterson, M. D., and Antcliff, K. R., "VTOL Urban Air Mobility Concept Vehicles for Technology Development," 2018 Aviation Technology, Integration, and Operations Conference, June 2018. DOI: 10.2514/6.2018-3847.
- 3. Saeed, A. S., Younes, A. B., Cai, C., and Cai, G., "A survey of hybrid Unmanned Aerial Vehicles," *Progress in Aerospace Sciences*, Vol. 98, April 2018, pp. 91–105. DOI: 10.1016/j.paerosci.2018.03.007.
- Kim, H. D., Perry, A. T., and Ansell, P. J., "A Review of Distributed Electric Propulsion Concepts for Air Vehicle Technology," 2018 AIAA/IEEE Electric Aircraft Technologies Symposium, July 2018. DOI: 10.2514/6.2018-4998.
- 5. Johnson, W., and Silva, C., "NASA Concept Vehicles and the Engineering of Advanced Air Mobility Aircraft," *The Aeronautical Journal*, Vol. 126, (1295), January 2022, pp. 59–91. DOI: 10.1017/aer.2021.92.
- 6. "eVTOL Aircraft Directory," *Electric VTOL News*TM, https://evtol.news/aircraft, Accessed 02 March 2025.
- Hirschberg, M., "Press Release: Vertical Flight Society Electric VTOL Directory Hits 1,100 Designs," https://evtol.news/news/press-release-vertical-flight-society-electric-vtol-directory-hits-1100-designs, Accessed 22 March 2025.

- 8. Murphy, P. C., Buning, P. G., and Simmons, B. M., "Rapid Aero Modeling for Urban Air Mobility Aircraft in Computational Experiments," AIAA SciTech 2021 Forum, January 2021. DOI: 10.2514/6.2021-1002.
- Simmons, B. M., Buning, P. G., and Murphy, P. C., "Full-Envelope Aero-Propulsive Model Identification for Lift+Cruise Aircraft Using Computational Experiments," AIAA AVIATION 2021 Forum, August 2021. DOI: 10.2514/6.2021-3170.
- Busan, R. C., Rothhaar, P. M., Croom, M. A., Murphy, P. C., Grafton, S. B., and O'Neal, A. W., "Enabling Advanced Wind-Tunnel Research Methods Using the NASA Langley 12-Foot Low Speed Tunnel," 14th AIAA Aviation Technology, Integration, and Operations Conference, June 2014. DOI: 10.2514/6.2014-3000.
- Murphy, P. C., and Landman, D., "Experiment Design for Complex VTOL Aircraft with Distributed Propulsion and Tilt Wing," AIAA Atmospheric Flight Mechanics Conference, January 2015. DOI: 10.2514/6.2015-0017.
- Busan, R. C., Murphy, P. C., Hatke, D. B., and Simmons, B. M., "Wind Tunnel Testing Techniques for a Tandem Tilt-Wing, Distributed Electric Propulsion VTOL Aircraft," AIAA SciTech 2021 Forum, January 2021. DOI: 10.2514/6.2021-1189.
- Simmons, B. M., and Murphy, P. C., "Aero-Propulsive Modeling for Tilt-Wing, Distributed Propulsion Aircraft Using Wind Tunnel Data," *Journal of Aircraft*, Vol. 59, (5), September 2022, pp. 1162–1178. DOI: 10.2514/1.C036351.
- Simmons, B. M., Morelli, E. A., Busan, R. C., Hatke, D. B., and O'Neal, A. W., "Aero-Propulsive Modeling for eVTOL Aircraft Using Wind Tunnel Testing with Multisine Inputs," AIAA AVIATION 2022 Forum, June 2022. DOI: 10.2514/6.2022-3603.
- Simmons, B. M., and Busan, R. C., "Statistical Wind-Tunnel Experimentation Advancements for eVTOL Aircraft Aero-Propulsive Model Development," AIAA SciTech 2024 Forum, January 2024. DOI: 10.2514/6.2024-2482.
- Simmons, B. M., Ackerman, K. A., and Asper, G. D., "Aero-Propulsive Damping Characterization for eV-TOL Aircraft Using Free Motion Wind-Tunnel Testing," AIAA SciTech 2025 Forum, January 2025. DOI: 10.2514/6.2025-0006.
- 17. Simmons, B. M., "System Identification Approach for eVTOL Aircraft Demonstrated Using Simulated Flight Data," *Journal of Aircraft*, Vol. 60, (4), July 2023, pp. 1078–1093. DOI: 10.2514/1.C036896.

- 18. Simmons, B. M., Rapsomanikis, A., Jacobellis, G., Ofodile, N., Hamilton, T., and Ma, M., "Flight-Test System Identification Methodology and Hover Results for a Vectored-Thrust eVTOL Aircraft," Vertical Flight Society's 81st Annual Forum & Technology Display, May 2025, To be published.
- Cook, J., and Gregory, I., "A Robust Uniform Control Approach for VTOL Aircraft," VFS Autonomous VTOL Technical Meeting and Electric VTOL Symposium, January 2021.
- Acheson, M. J., Gregory, I. M., and Cook, J., "Examination of Unified Control Incorporating Generalized Control Allocation," AIAA SciTech 2021 Forum, January 2021. DOI: 10.2514/6.2021-0999.
- Milz, D., May, M. S., and Looye, G., "Dynamic Inversion-Based Control Concept for Transformational Tilt-Wing eVTOLs," AIAA SciTech 2024 Forum, January 2024. DOI: 10.2514/6.2024-1290.
- Comer, A., and Chakraborty, I., "Total Energy-Based Control Design and Optimization for Lift-Plus-Cruise Aircraft," *Journal of Guidance, Control, and Dynamics*, Vol. 47, (7), July 2024, pp. 1414–1436. DOI: 10.2514/1.G007605.
- 23. Comer, A. M., and Chakraborty, I., "Full Envelope Flight Control System Design and Optimization for a Tilt-Wing Aircraft," *Journal of the American Helicopter Society*, Vol. 69, (3), July 2024, pp. 1–18. DOI: 10.4050/JAHS.69.032003.
- Comer, A. M., "Optimizing Explicit Model-Following Trajectory Control Laws for a Vectored Thrust Conguration," *Journal of the American Helicopter Society*, Vol. 70, (1), January 2025, pp. 1–20. DOI: 10.4050/JAHS.70.012007.
- Geuther, S. C., Simmons, B. M., and Ackerman, K. A.,
 "Overview of the Subscale RAVEN Flight Controls and Modeling Testbed," Vertical Flight Society's 80th Annual Forum & Technology Display, May 2024.
- German, B. J., Jha, A., Whiteside, S. K. S., and Welstead, J. R., "Overview of the Research Aircraft for eVTOL Enabling techNologies (RAVEN) Activity," AIAA AVIATION 2023 Forum, June 2023. DOI: 10.2514/6.2023-3924.
- "NASA Langley 12-Foot Low-Speed Tunnel," https://researchdirectorate.larc.nasa.gov/12-footlow-speed-tunnel-12-ft-lst/, Accessed 17 September 2024.
- 28. Rothhaar, P. M., Murphy, P. C., Bacon, B. J., Gregory, I. M., Grauer, J. A., Busan, R. C., and Croom, M. A., "NASA Langley Distributed Propulsion VTOL

- Tilt-Wing Aircraft Testing, Modeling, Simulation, Control, and Flight Test Development," 14th AIAA Aviation Technology, Integration, and Operations Conference, June 2014. DOI: 10.2514/6.2014-2999.
- McSwain, R. G., Geuther, S. C., Howland, G., Patterson, M. D., Whiteside, S. K., and North, D. D., "An Experimental Approach to a Rapid Propulsion and Aeronautics Concepts Testbed," NASA TM-2020-220437, January 2020.
- North, D. D., Busan, R. C., and Howland, G., "Design and Fabrication of the Langley Aerodrome No. 8 Distributed Electric Propulsion VTOL Testbed," AIAA SciTech 2021 Forum, January 2021. DOI: 10.2514/6.2021-1188.
- Cooper, J. R., Ackerman, K. A., Rothhaar, P. M., and Gregory, I. M., "Autonomous Path-Following for a Tilt-Wing, Distributed Electric Propulsion, Vertical Take-Off and Landing Unmanned Aerial System in Hover Mode," NASA TM-2018-220109, November 2018.
- 32. McSwain, R. G., Glaab, L. J., and Theodore, C. R., "Greased Lightning (GL-10) Performance Flight Research Flight Data Report," NASA TM–2017–219794, November 2017.
- Fredericks, W. J., McSwain, R. G., Beaton, B. F., Klassman, D. W., and Theodore, C. R., "Greased Lightning (GL-10) Flight Testing Campaign," NASA TM-2017–219643, July 2017.
- Geuther, S. C., and Fei, X., "LA-8 Computational Analysis and Validation Studies Using Flight-Stream," AIAA SciTech 2021 Forum, January 2021. DOI: 10.2514/6.2021-1191.
- 35. Ahuja, V., and Hartfield, R. J., "Reduced-Order Aerodynamics with the Method of Integrated Circulation," AIAA SciTech 2022 Forum, January 2022. DOI: 10.2514/6.2022-0005.
- DiMaggio, G. A., Simmons, B. M., Geuther, S. C., Hartfield, R. J., and Ahuja, V., "Transition Aero-Propulsive Analysis of a Tilt-Wing eVTOL Aircraft Using a Surface-Vorticity Solver," AIAA SciTech 2025 Forum, January 2025. DOI: 10.2514/6.2025-0654.
- 37. Geuther, S. C., North, D. D., and Busan, R. C., "Investigation of a Tandem Tilt-Wing VTOL Aircraft in the NASA Langley 12-Foot Low-Speed Tunnel," NASA TM–2020–5003178, June 2020.
- 38. Simmons, B. M., and Hatke, D. B., "Investigation of High Incidence Angle Propeller Aerodynamics for Subscale eVTOL Aircraft," NASA TM–20210014010, May 2021.

- 39. Simmons, B. M., "System Identification for Propellers at High Incidence Angles," *Journal of Aircraft*, Vol. 58, (6), November 2021, pp. 1336–1350. DOI: 10.2514/1.C036329.
- Stratton, M., and Landman, D., "Wind Tunnel Test and Empirical Modeling of Tilt-Rotor Performance for eV-TOL Applications," AIAA SciTech 2021 Forum, January 2021. DOI: 10.2514/6.2021-0834.
- 41. Simmons, B. M., "Evaluation of Response Surface Experiment Designs for Distributed Propulsion Aircraft Aero-Propulsive Modeling," AIAA SciTech 2023 Forum, January 2023. DOI: 10.2514/6.2023-2251.
- 42. Simmons, B. M., "Efficient Variable-Pitch Propeller Aerodynamic Model Development for Vectored-Thrust eVTOL Aircraft," AIAA AVIATION 2022 Forum, June 2022. DOI: 10.2514/6.2022-3817.
- Simmons, B. M., Geuther, S., and Ahuja, V., "Validation of a Mid-Fidelity Approach for Aircraft Stability and Control Characterization," AIAA AVIATION 2023
 Forum, June 2023. DOI: 10.2514/6.2023-4076.
- 44. Montgomery, D. C., *Design And Analysis of Experiments*, John Wiley & Sons, Inc., Hoboken, NJ, 8th edition, 2013.
- 45. Myers, R. H., Montgomery, D. C., and Anderson-Cook, C. M., Response Surface Methodology: Process and Product Optimization Using Designed Experiments, John Wiley & Sons, Hoboken, NJ, fourth edition, 2016.
- 46. Vicroy, D. D., Loeser, T. D., and Schütte, A., "Static and Forced-Oscillation Tests of a Generic Unmanned Combat Air Vehicle," *Journal of Aircraft*, Vol. 49, (6), November 2012, pp. 1558–1583. DOI: 10.2514/1.C031501.
- 47. Vicroy, D. D., "A Guide to Forced Oscillation Data Processing and Analysis," NASA TP–20210023569, June 2023.
- 48. "Flight Dynamics Simulation of a Generic Transport Model," NASA Technology Transfer Program, https://software.nasa.gov/software/LAR-17625-1, Accessed 17 September 2024.
- 49. "MathWorks Documentation," https://www.mathworks.com/help/, Accessed 01 March 2025.
- 50. "X-Plane," https://www.x-plane.com/, Accessed 22 March 2025.
- Comer, A. M., Simmons, B. M., and Asper, G. D., "Design, Simulation, and Flight Testing of a Multi-Purpose VTOL Flight Control System," NASA TM-20250000954, To be published.

- Fritsch, F. N., and Carlson, R. E., "Monotone Piecewise Cubic Interpolation," SIAM Journal on Numerical Analysis, Vol. 17, (2), 1980, pp. 238–246.
 DOI: 10.1137/0717021.
- Moler, C. B., Numerical Computing with MATLAB, Society for Industrial and Applied Mathematics, Philadelphia, PA, January 2004. DOI: 10.1137/1.9780898717952.
- 54. Morelli, E. A., and Klein, V., *Aircraft System Identification: Theory and Practice*, Sunflyte Enterprises, Williamsburg, VA, second edition, 2016.
- 55. Etkin, B., and Reid, L. D., *Dynamics of Flight: Stability and Control*, John Wiley & Sons, Inc, New York, NY, third edition, 1996.
- Stevens, B. L., Lewis, F. L., and Johnson, E. N., Aircraft Control and Simulation: Dynamics, Controls Design, and Autonomous Systems, John Wiley & Sons, Hoboken, NJ, third edition, 2015.
- Pei, J., and Roithmayr, C., "Equations of Motion for a Generic Multibody Tilt-rotor Aircraft," AIAA AVIA-TION 2022 Forum, June 2022. DOI: 10.2514/6.2022-3511.
- 58. "U.S. Standard Atmosphere," NOAA–S/T 76–1562, October 1976.
- Johnson, D. L., "Terrestrial Environment (Climatic) Criteria Guidelines for Use in Aerospace Vehicle Development, 1993 Revision," NASA TM-4511, August 1993.
- 60. "Flying Qualities of Piloted Aircraft," MIL-STD-1797A, January 1990.
- 61. Chen, C.-T., *Linear System Theory and Design*, Oxford University Press, fourth edition, 2014.
- Young, P. C., and Willems, J., "An Approach to the Linear Multivariable Servomechanism Problem," *International Journal of Control*, Vol. 15, (5), 1972, pp. 961–979.
- 63. Berger, T., "Handling Qualities Requirements and Control Design for High-Speed Rotorcraft," Special Report FCDD-AMV-20-01, February 2020.
- Enns, D., "Control Allocation Approaches," Guidance, Navigation, and Control Conference and Exhibit, August 1998. DOI: 10.2514/6.1998-4109.
- 65. Acheson, M. J., and Gregory, I. M., "Modified Cascading Generalized Inverse Control Allocation," AIAA SciTech 2023 Forum, January 2023. DOI: 10.2514/6.2023-2542.
- 66. Berger, T., Tischler, M. B., Hagerott, S. G., Gangsaas, D., and Saeed, N., "Longitudinal Control Law Design and Handling Qualities Optimization for a Business Jet Flight Control System," AIAA Guidance,

- Navigation and Control Conference, August 2012. DOI: 10.2514/6.2012-4503.
- 67. Stoll, A., and Bevirt, J., "Development of eVTOL Aircraft for Urban Air Mobility at Joby Aviation," Vertical Flight Society's 78th Annual Forum & Technology Display, May 2022. DOI: 10.4050/F-0078-2022-17528.
- 68. Jategaonkar, R. V., *Flight Vehicle System Identification: A Time-Domain Methodology*, American Institute of Aeronautics and Astronautics, Reston, VA, second edition, 2015. DOI: 10.2514/4.102790.
- 69. Tischler, M. B., and Remple, R. K., *Aircraft and Rotor-craft System Identification: Engineering Methods With Flight Test Examples*, American Institute of Aeronautics and Astronautics, Reston, VA, second edition, 2012. DOI: 10.2514/4.868207.
- "System IDentification Programs for AirCraft (SID-PAC)," NASA Technology Transfer Program, https://software.nasa.gov/software/LAR-16100-1, Accessed 08 November 2024.
- 71. Morelli, E. A., "Multiple Input Design for Real-Time Parameter Estimation in the Frequency Domain," 13th IFAC Conference on System Identification, August 2003. DOI: 10.1016/S1474-6670(17)34833-4.
- 72. Morelli, E. A., "Flight-Test Experiment Design for Characterizing Stability and Control of Hypersonic Vehicles," *Journal of Guidance, Control, and Dynamics*, Vol. 32, (3), May 2009, pp. 949–959. DOI: 10.2514/1.37092.
- Morelli, E. A., "Practical Aspects of Multiple-Input Design for Aircraft System Identification Flight Tests," AIAA AVIATION 2021 Forum, August 2021. DOI: 10.2514/6.2021-2795.
- Grauer, J. A., and Boucher, M., "System Identification of Flexible Aircraft: Lessons Learned from the X-56A Phase 1 Flight Tests," AIAA SciTech 2020 Forum, January 2020. DOI: 10.2514/6.2020-1017.
- Asper, G. D., and Simmons, B. M., "Rapid Flight Control Law Deployment and Testing Framework for Subscale VTOL Aircraft," NASA TM-20220011570, September 2022.
- Asper, G. D., Simmons, B. M., Axten, R. M., Ackerman, K. A., and Corrigan, P. E., "Inexpensive Multirotor Platform for Advanced Controls Testing (IMPACT): Development, Integration, and Experimentation," NASA TM–20240000223, March 2024.
- 77. "PX4 Autopilot User Guide," https://docs.px4.io/main/en/, Accessed 11 March 2025.
- 78. "uORB Messaging," https://docs.px4.io/main/en/middleware/uorb.html, Accessed 18 April 2024.

- Simmons, B. M., Gresham, J. L., and Woolsey, C. A., "Flight-Test System Identification Techniques and Applications for Small, Low-Cost, Fixed-Wing Aircraft," *Journal of Aircraft*, Vol. 60, (5), September 2023, pp. 1503–1521. DOI: 10.2514/1.C037260.
- 80. "QGroundControl," https://qgroundcontrol.com/, Accessed 23 March 2025.
- 81. DroneCAN, "DroneCAN Documentation," https://dronecan.github.io/, Accessed 18 April 2024.
- 82. "ULog File Format," https://docs.px4.io/main/en/dev_log/ulog_file_format.html, Accessed 12 March 2025.
- 83. "GitLab," https://about.gitlab.com/, Accessed 09 March 2025.